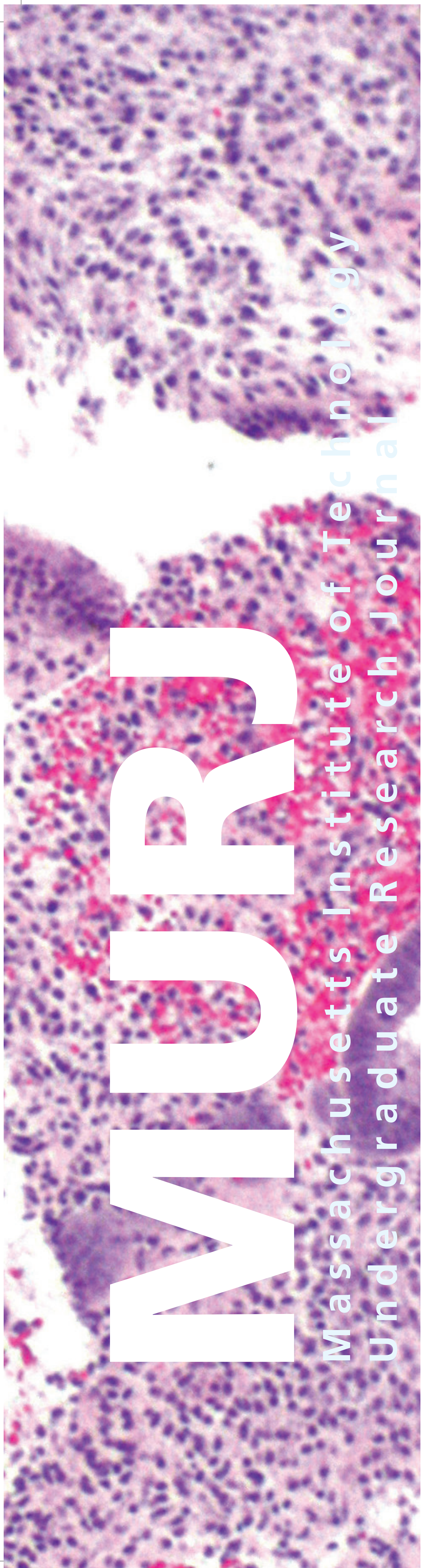
MURJ
Massachusetts Institute of Technology
Undergraduate Research Journal

Contents

MURJ Staff
MIT Undergraduate Research Journal

Massachusetts Institute of Technology

December 2016

Dear MIT community,

We are excited to publish the 32nd issue of the MIT Undergraduate Research Journal, a biannual student-run publication that features diverse and groundbreaking undergraduate research happening across campus. For the past 16 years, MURJ has been an emblem of the intellectual curiosity and passion of MIT undergraduates, and this semester's issue is certainly no exception. Here, we present research articles covering a diverse range of topics, including using ultrasonic techniques to more accurately predict the service life of aircraft engines, the creation of a cost-effective rechargeable battery for underwater vehicles that collect ocean data, and a new model for classifying galaxies that will help scientists better understand their evolution. You will also read short summaries of UROP projects currently being conducted by MIT students, such as a study that tests and characterizes noble gases to better inform particle physics experiments, as well as a study that aims to create a synthetic mimic of the chlorosome, the light harvesting system found in plants.

In addition to our research articles, we also present insightful features articles that explore exciting scientific topics and happenings around the Institute. In this issue, we look at the potential of CRISPR as a gene-editing technology, and what that might look like at the population level. In addition, we also take a look at this year's iGEM competition, and how a team of MIT students used synthetic biology to tackle endometriosis.

Massachusetts Institute of Technology

MURJ Staff
MIT Undergraduate Research Journal

Biannual publication of this journal is a collaborative undertaking by an extraordinary team of dedicated students. We would like to thank our editorial board and contributors for their time and hard work this semester. In addition, we would like to thank all of the undergraduates who shared their research with us and the greater MIT community.

For previous issues of the MIT Undergraduate Research Journal, please visit our website at murj.mit.edu. If you are interested in contributing to future issues of the MIT Undergraduate Research Journal, we invite you to join our team of authors and editors or submit your research for our Spring 2017 issue. Please contact murj-officers@mit.edu if you have any questions or comments.

Best,

Elena Polozova
(Co-Editor-in-Chief)

Daphne Superville
(Co-Editor-in-Chief)

Massachusetts Institute of Technology

UNDERGRADUATE RESEARCH JOURNAL
Volume 32, Fall 2016

TECHNOLOGY

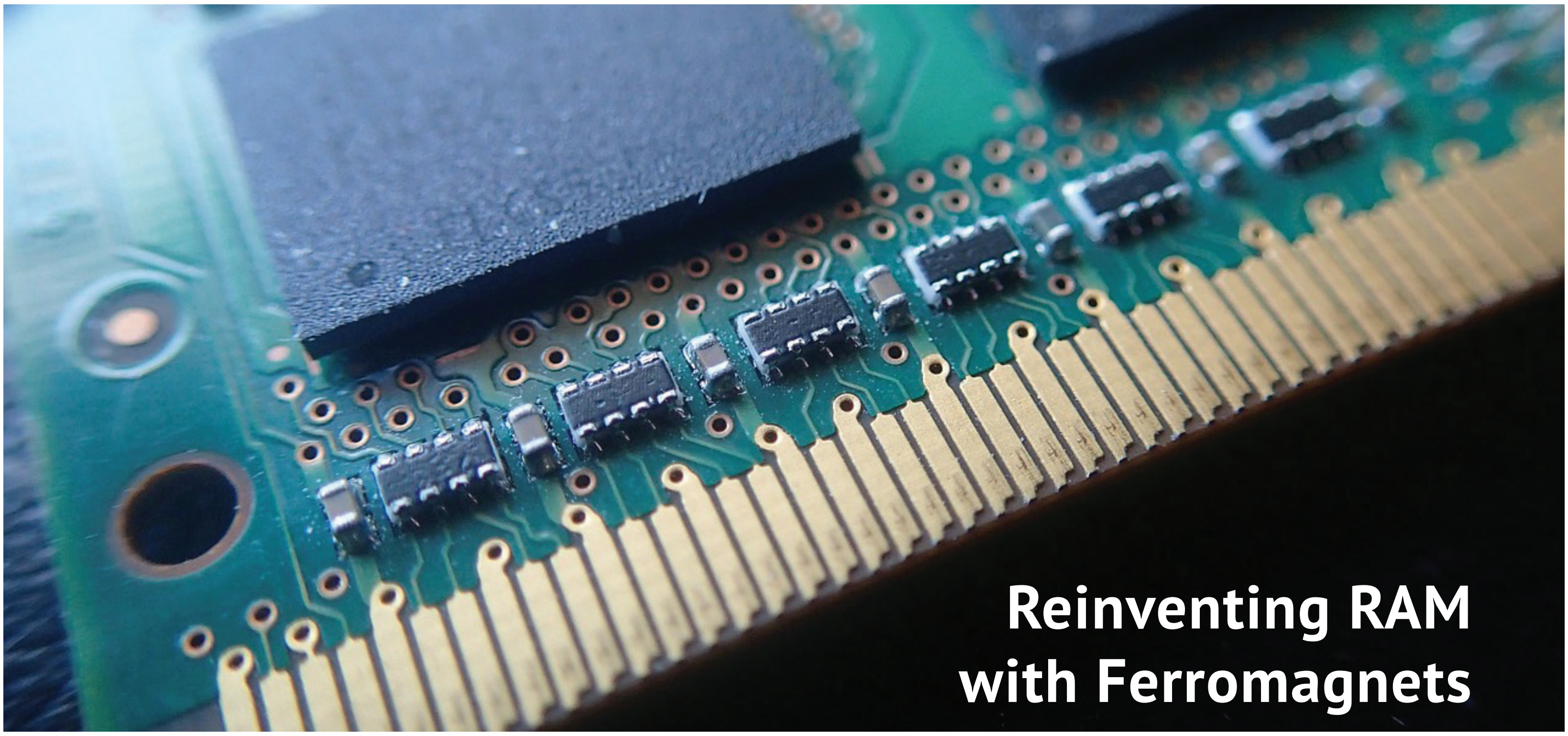

Reinventing RAM with Ferromagnets

Thanks to 2D materials innovation, RAM might soon look quite different. Along with collaborators at Tsinghua University, MIT researchers have found a large bandgap and ferroelectricity at surprisingly high temperature in SnTe (tin-tellurium) in the form of films only a few atoms thick.

SnTe is a semiconductor that changes its structure and becomes ferroelectric at a transition temperature. Ferromagnetic materials have a spontaneous polarization (segregation of positive and negative charges) that can be reversed by an electric field. In bulk SnTe, the highest recorded transition temperature is only 98 K. But in thin films, where the material is only a few unit cells thick, researchers from MIT and Tsinghua University have found something very different -- transition temperatures near room temperature. This higher temperature could allow for many commercial applications.

The study found that SnTe hin-films 2-4 unit cells thick were ferroelectric up to 80 °F , the highest they were capable of measuring. This trend is the opposite of what has been observed in other materials. "This discovery is very exciting because usually when you decrease the thickness from the 3-D to 2-D, the phase transition temperature always decreases and therefore could destroy the ferroelectricity. But in this case, the [ferroelectric] phase transition temperature increased. It's quite unusual," says MIT postdoc Junwei Liu.

The small signal from thin-films required more sensitive measurements than the typical methods offer, which made data collection challenging. To get around this, the group used scanning tunneling microscopy (STM) and scanning tunneling spectroscopy (STS) to observe signs of ferroelectricity such as lattice distortion and band bending. Researchers were also able to tune the polarization of the films with an applied electric field, the main characteristic of ferroelectric materials.

The unusual ferroelectricity in SnTe thin films may be explained by a drop in the density of Sn vacancies and an increase in bandgap, the energy range where there are no electrons. In ultrathin films, the number of Sn vacancies drops by 2 to 3 orders of magnitude, decreasing the number of free carriers. The bandgap in these films is also eight times higher than in the bulk material. These two factors cause the transition temperature to increase.

Based on this finding, the researchers propose a Ferroelectric Random Access Memory device. In these devices, the two polarization states are considered as "on" and "off" or 0 and 1. Previous ferroelectric RAM had the drawback of having to destroy a state in order to read it, but the new proposal, based on in-plane polarization and electron tunneling, avoids that, making the device more efficient than other ferroelectric RAM devices. To write a state, the device applies a voltage that flips the in-plane polarization of the SnTe film to switch between on and off. These states are read by electron tunneling.

The next steps towards the creation of a Ferroelectric RAM device are demonstrating room-temperature ferroelectricity within a prototype and figuring out how to cost-effectively synthesize high-quality SnTe thin-films. Additional potential applications for these films include nanosensors and electronics, which could benefit from the films' room temperature ferroelectricity.

— J. Hines

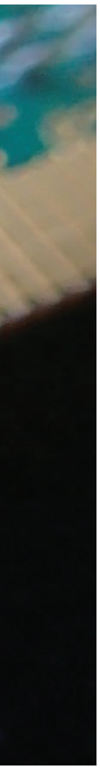

EMOTION

Wireless Technology Detecting Our Hidden Emotions

Ever wondered what emotions were hiding behind a poker face? How could anyone truly tell? Emotions, one of the most characteristically complex phenomena of the human condition, can now be detected through wireless signals. Building machines that can sense emotional states (happy, sad, angry, pleased…etc.) has a wide range of applications from interactive smart homes to detection of psychological diseases such as depression, anxiety, and bipolar disorder. Existing approaches to detecting emotions rely on audiovisual cues such as reading facial expressions or an electrocardiography (ECG) monitor. Audiovisual cues can be lacking in measuring inner feelings such as depression, whereas ECG monitoring can be cumbersome due to use of body sensors.

87%
Accuracy reached by EQ-Radio

EQ-Radio, developed by the Katabi Lab at the MIT Computer Science and Artificial Intelligence Lab (CSAIL), overcomes obstacles caused by both of these technologies by measuring physiological signals, which fluctuate with changes in emotional state, without body contact. This design uses three components to fully recognize emotions: a radio that transmits and receives reflections of radio frequency (RF) signals that bounce off the human body, a new algorithm that extracts individual heartbeats from RF signals, and an emotion classification sub-system that analyzes the heartbeats and breathing patterns to differentiate among different emotional states. One of the most integral parts of this project is the development of the algorithm, which first mitigates the impact of breathing to emphasize the heartbeat, and then captures individual heartbeats by segmenting the RF reflections. Comparing EQ-Radio data with that of ECG shows that EQ-Radio accurately identified emotions 87% of the time with at most 1.2 percentage points behind ECG's level of accuracy. For the first time, these preliminary tests of EQ-Radio demonstrate the feasibility of wirelessly identifying emotion using RF reflections, advancing the field of emotion detection by broadening the possibility of machines to interact with people rather than solely executing explicit commands.

—Zuly M.

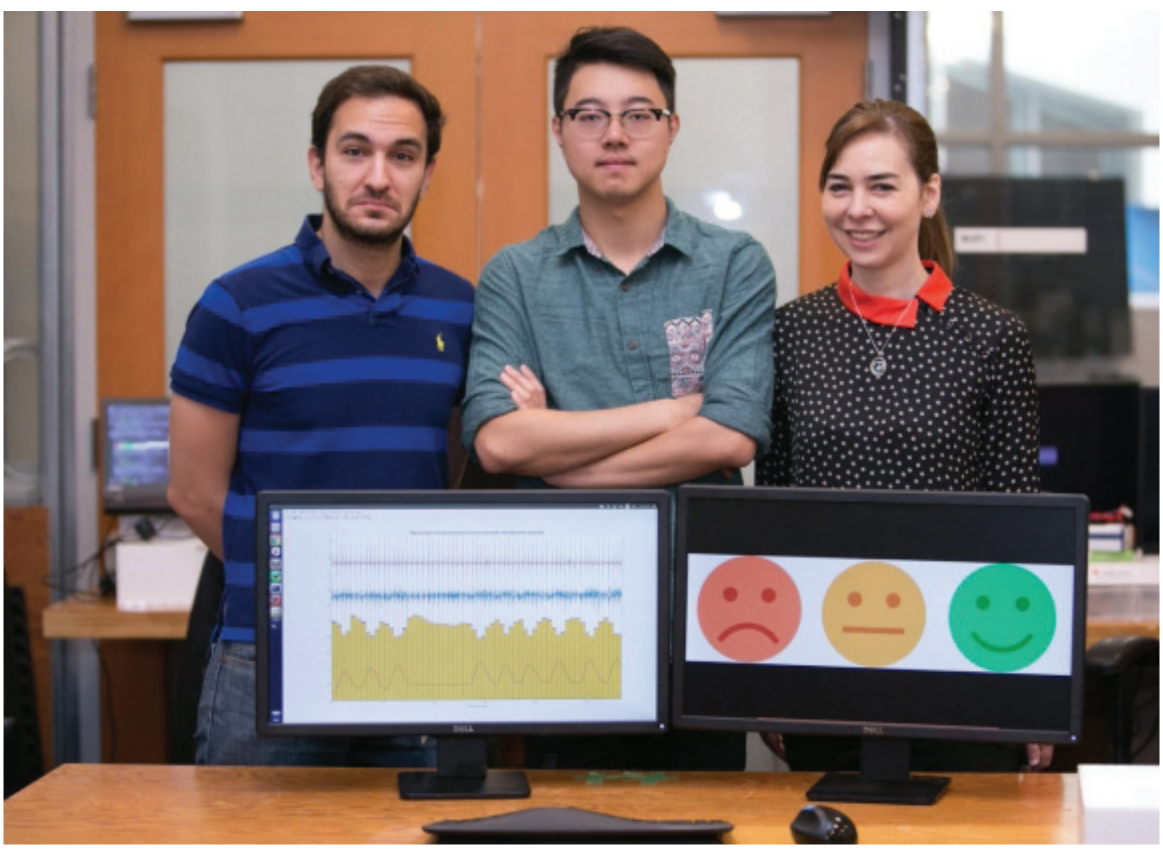

MIT News Notes: Left to right: PhD student Fadel Adib, PhD student Mingmin Zhao, and Professor Dina Katabi pose with their EQ-Radio device, which can detect emotion using wireless signals.

(Source: MITCSAIL, Photo credit: Jason Dorfman)

Artifical Intellegence

Shock-absorbing Tech in 3D Printed Robotic Jumping Cubes

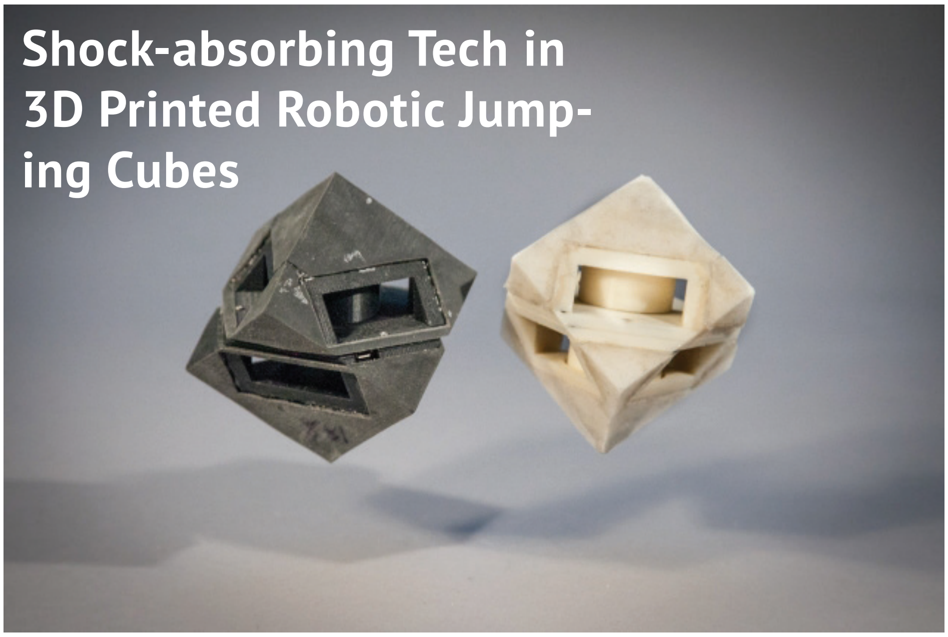

CSAIL team develops printed dampening materials for customizable, durable properties in robots.

MIT researchers outfitted their cube robot with shock-absorbing "skins" that transfer less than half of the energy that would normally be transferred to the ground.
(Source: MIT CSAIL, Photo credit: Jason Dorfman)

As the realm of small and soft robotics increases, there's been more of a push to integrate drones, small mechanics, and personal robots into everyday life. Continued improvement in additive manufacturing – 3D printing – has engineers and manufacturers finding that the affordability and speed of production printers offer could change the way they develop robots.

In early October, a group of Computer Science and Artificial Intelligence Laboratory (CSAIL) researchers refined a method of 3D printing viscoelastic materials for use as dampeners and skins in robotics. "Programmable Viscoelastic Materials" (PVM) as they call them, are made from a form of additive manufacturing that mixes solid and liquid printing techniques and can make the product's properties completely customizable. Designers can make the material as stiff, as elastic, or as shock-absorbing as needed in the same print-job, and can have these properties be variable on the same product.

The researchers found that the technology can be effective as dampers, which are energy-absorbing materials that can serve as 'vibration isolators,' or shells that protect sensitive electronics from motors or impacts. Similar methods have been used before to minimize damage to parts, and classic dampening materials are widely used to distribute and minimize the effect of vibrations and movement on a robotic system. However, these classic materials have always had their setbacks and limitations. Commercially available dampeners are only available in certain dimensions and properties, and when obtained, will still

> "The cubes use only 1/250 the amount of energy absorbed into the ground, and precision on landing went up by a factor of four."

need to be altered further by molding or shaping – processes that take up time and money.

The group configured a standard inkjet 3D printer to perform the necessary new processes. They had previously discovered how to modify these printers to simultaneously print solids and liquids, and to deposit selected materials in varying densities. Then, the research team designed practical constraints for variables and algorithms for testing and observing the product's "bounce" and precision on landing.

Protective covering for small robots could be developed with the use of the impact absorption skins. The materials were printed in the form of cubes that contain motors, actuators, and a metal spring band. Researchers found that the cubes use only 1/250 the amount of energy absorbed into the ground, and precision on landing went up by a factor of four. The results show that the skin could be used to protect phones, drones, cameras, and other delicate devices. It could also be useful in other types of high force technologies like helmets and running shoes. According to the authors of the study, this new technology could allow for fewer limitations on robotic design, as well as the design of several other products.

—K. Hinojosa

Cancer Treatment

Predicting the Outcome of Cancer Treatments

Unlike other diseases, treating cancer does not follow a "one size fits all" methodology. Whether a chemotherapeutic drug is successful will vary tremendously on a case-to-case basis. In order to improve patient outcomes, a large amount of research has been geared towards trying to combat cancer with personalized medicine - where a patient's treatment is individually tailored based on his or her genetic makeup.

A recent development from scientists at MIT and Dana-Farber Cancer Institute seems to bring individualized cancer treatment closer to reality. In a paper published in Nature Biotechnology, researchers from these institutions describe an assay that can be used to determine whether a tumor will be susceptible to a drug or not.

By using a suspended microchannel resonator (SMR), a device developed at the Manalis Lab at MIT, researchers were able to calculate the growth rates of individual tumor cells over a period of time in the presence of absence of a drug. They sought to determine whether the susceptibility of tumor cells to a drug correlates with changes in the growth rate.

Not all patients react equally to the same chemotherapeutic drug. Response and resistance to treatment varies from patient to patient.
(Image Source: Wikimedia)

By measuring the growth rate of tumor cell lines in the presence of drugs that had been previously reported to be effective or ineffective, they confirmed that, when cancerous cells are exposed to drugs to which they are sensible, their growth rate is affected. Thus, by using this assay and measuring the growth rate of a patient's tumor cells in the presence of different drugs, physicians rapidly can predict to which drugs the tumor will be susceptible. Advances such as this one pave the way towards a future where personalized medicine is the standard methodology of care.

—S. Santiago

Enviromental Engineering

Adaptive Radiation in Microbes

Adaptive radiation is a process that occurs when a clade of organisms, those which are believed to have evolved from a common ancestor, rapidly differentiate to fill niches opened up by an ecological opportunity. From finches in the Galapagos Islands to cichlid fish in Lake Victoria, examples of adaptive radiations in plant and animal populations are found around the world. However, adaptive radiations in microbes in the wild have proved difficult to document.

MIT researchers from the Department of Civil and Environmental Engineering described an instance of microbial adaptive radiation in the alginate degradation pathways of populations of marine bacteria belonging to the Vibrionaceae family. A study published in the journal Nature Communications and led by Jan-Hendrik Hehemann, Philip Arevalo, and Manoshi S. Datta used closely related Vibrionaceae isolates, including a single clade of seven recently diverged populations referred to in the study as the "crown group." The isolates specialized in the degradation of different forms of the same algal glycan, a food source for the Vibrionaceae that they must break down before using. Specialization was based on the presence or absence in the microbe of enzymes used in the degradation pathway, including alginate lyases (Aly) and oligoalginate lyases (Oal).

Image of Vibrio cholerae, bacteria belonging to the same genus as those used in the study.
(Source: Wikimedia, Photo credit: Tom Kirn)

The researchers investigated how the clade of vibrios differentiated by constructing a phylogenetic tree, a prediction of the evolutionary relationships between species based on their ribosomal proteins and nucleotide sequences. This detailed phylogenetic reconstruction revealed that adaptive radiation leading to differentiated degradation pathways was driven by horizontal gene transfer to the extent that every population in the study had exchanged at least one copy of Oal genes with another population. This phylogenetic evidence rejects the idea that a distant ancestor acquired the core pathway and that the pathway was modified as the clade evolved and differentiated. The rapidness of adaptive radiation driven by horizontal gene transfer is evident in the crown group of vibrios. Some populations within the crown group had lost the entire alginate degradation pathway while others had acquired an additional range of Aly genes, despite the fact that the populations diverged recently enough to possess nearly identical ribosomal protein sequences.

"The creation of such an organism highlights the potential use of ***fine-scale physiological differences*** in microbes as a resource for bioengineering."

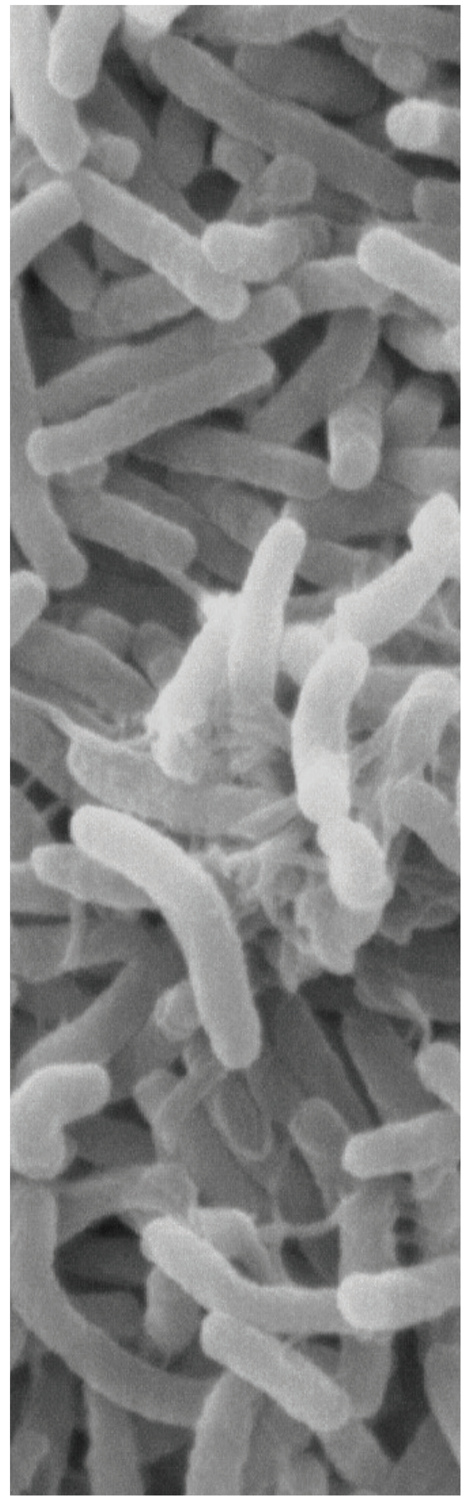

Image of Vibrio cholerae
(Source: Wikimedia , Photo credit: Ronald Taylor)

The differentiated pathways of the vibrios enabled them to develop different ecophysiological strategies. Strains that possessed at least one Aly and Oal enzyme family were able to grow on polymeric forms of alginate because of their ability to degrade algal glycans with a high molecule weight into usable parts. Some colonies in plate-based assays even broadcast halos of enzyme activity beyond the colony boundary, allowing them to act as "pioneers" able to colonize native substances. Strains that lacked Aly families ("scavengers") or whose Aly enzymes were tethered to the cell rather than broadcast ("harvesters") took advantage of the oligomers already partially degraded by pioneer species. Further work is necessary to determine how stable the degradation cascade comprising these three ecophysiological types is in the wild.

Some pioneer species with particularly large halos of enzyme activity and a superior ability to degrade polymeric alginate were "super broadcasters." A similar super broadcaster was engineered by the Bio Architecture Lab, a biotechnology company, to produce bioethanol from algae. According to the authors of the MIT study, the creation of such an organism highlights the potential use of fine-scale physiological differences in microbes, like those resulting from bursts of adaptive radiation, as a resource for bioengineering.

—A. Huske

The Search For Dark Matter

ABRACADABRA: the Magical Potential of Axions

MIT Researchers have developed a prototype device called ABRACADABRA in hope of detecting axions, a possible explanation for dark matter.

In the search for dark matter, re-searchers have become interested in axions, theoretical particles that would be important to both cosmology and quantum chromodynamics (QCD) if discovered. These particles are of interest because they are highly lightweight and would be able to explain why we have been unable to detect dark matter beforehand, as well as provide a proposed solution to the question of why in QCD the physical laws remain the same when charge signs and orientation are switched.

At the Laboratory of Nuclear Science (LNS), MIT Associate Professor Jesse Thaler, MIT Pappalardo Fellow Benjamin Safdi, and Yonatan Kahn PhD '15, are creating an axion-detection device called ABRACADABRA (A Broadband/Resonant Approach to Cosmic Axion Detec-

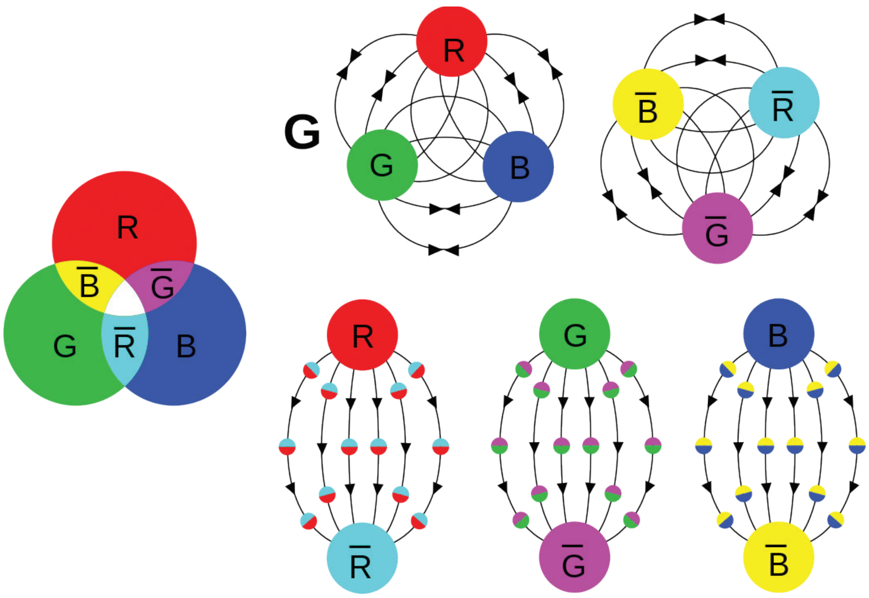

Top Right: Quantum chromodynamics describes the interactions of the strong force. It specifies allowable particle interactions based on the 'color' of the particles involved. (Source: Wikimedia, Photo credit: Maschen)

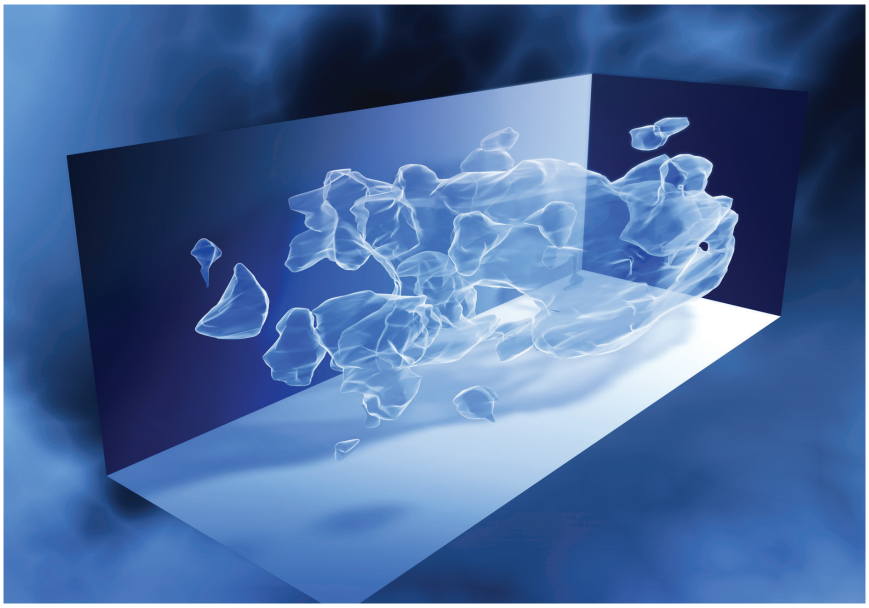

Bottom Right: A three-dimensional map depicting large-scale distribution of dark matter, an invisible form of matter that accounts for most of the Universe's mass. (Source: Wikimedia, Photo credit: NASA, Richard Massey) tion with an Amplifying B-field Ring Apparatus). This device will form a powerful static magnetic field, similar to that in a magnetar. When an axion collides with the field, it will create an effective current. This current will in turn create an oscillation in the field proportional to the Compton wavelength that can then be detected.

The static field will be created through the use of a superconducting toroid. A loop will be placed in the middle of the toroid to detect changes in the magnetic field. One proposed configuration for the inner loop, the broadband method, consists of an untuned magnetometer that is connected to a superconducting loop. Such a method would be able to detect masses smaller than ever previously detected. A second proposed configuration, the resonant method, consists of a magnetometer with a capacitor attached. Its main benefit is that it will increase sensitivity for larger masses. Researchers expect that in combination, the two methods will be able to detect any axions with energies ranging from 10^{-14} to 10^{-6} eV. This expands the state-of-the-art range of detection, allowing a broader search for axions, extending into lower energy levels. Other existing experiments, such as the ADMX experiment, can only search for axions at a more restricted range of energies and are unable to detect anything below 10^{-9} eV. The device proposed by Thaler and his colleagues would improve our ability to detect these lightweight particles. If successfully detected, the axion will serve as a point for researchers to further explore the universe.

—E. Nolasco-Martinez

MURJ Features

iGEM Giant Jamboree
Every year at the Giant Jamboree, a photo is taken of all attending teams. This year's photo aimed to feature over 300 teams.
(Photo credit: iGEM HQ)

Synthetic Biology:

MIT for Women's Health at the iGEM Giant Jamboree

A team of MIT students used tools from synthetic biology to advance research for a much-needed nonsurgical diagnostic for endometriosis, a project that won them a gold medal at the international synbio competition this October.

BY THERESA MACHEMER

"In some ways, my generation made a mess of the world, with the economy and the environment," Randy Rettberg, president and founder of the International Genetically Engineered Machine (iGEM) Foundation, said in his opening remarks at the iGEM Giant Jamboree awards ceremony. "At iGEM, we're giving you [the students] the tools with synthetic biology to fix it all up." Rettberg considers synthetic biology and its ability to create and innovate at the molecular level to be the next defining technological advancement, following the industrial and informational revolutions. He calls this era the "matter revolution," and said "the goal of synthetic biology is to establish fluent control over matter- a technical revolution of the 21st century." Seeing the potential of synthetic biology, Rettberg founded iGEM, a collegiate and high school competition that provides an opportunity for upcoming biological engineers to get an in-depth look at the field of synthetic biology and the impact it could have in the near future. In 2016, over 300 teams flew into Boston from around the world to attend the Giant Jamboree from October 28-31 at the Hynes Convention Center, where they presented their work and celebrated the advancements made in synthetic biology that year.

The iGEM Foundation organizes the competition into three experience categories: high school, undergraduate, and overgraduate, each with 13 different tracks ranging from art to medicine to the environment. Teams compete within

At Right: MIT iGEM Team
Left to right: Wangui Mbuguiro, Trinh Nguyen, Sarah Caso, Elizabeth Strand, Julia Goupil, Damono Berman, Maya Kaul, Kathleen Brandes, Archis Bhandarkar, Colleen Foley, Theresa Machemer, Gizem Gumuskaya.
(Photo credit: Brian Teague)

At Bottom: MIT iGEM at the Giant Jamboree
Team members present their work to the crowd and the judges in the front row. Left to right: Damon Berman, Elizabeth Strand, Archis Bhandarkar, Theresa Machemer.
(Photo credit: Brian Teague)

their track, for specialized awards (i.e. Best Diagnostic), and also compete for the Grand Prize within their overall category. Teams nominated for the Grand Prize presented for all of iGEM in the Hynes auditorium on Monday, October 31.

MIT has hosted an iGEM team every year since the competition's inception in 2004, where they were one of only five teams. While the MIT teams' first projects began with building basic, modular sensors, recent groups have addressed world issues from biofuel production to Alzheimer's treatment. For the 2016 iGEM Giant Jamboree, the MIT team of eleven undergraduates and one graduate student, under faculty advisor Professor Ron Weiss and direct supervisor Brian Teague both of the MIT Center for Integrated Synthetic Biology, chose to bring synthetic biology into the realm of women's health by tackling endometriosis.

Endometriosis is a disease characterized by chronic, debilitating abdominal pain caused by lesions of tissue similar to the inner lining of the uterus, the endometrium, growing elsewhere in the body. It is incredibly pervasive- affecting 1 in 10 women- but like most gynecological conditions, it is not common knowledge. Endometriosis was brought to the attention of the MIT team member Wangui Mbuguiro, Class of 2017, who was motivated to address endometriosis because of personal experience. Having had gynecological problems of her own, Mbuguiro said she became interested topics like endometriosis and gynepathology and suggested the topic to the team during a round of brainstorming in January. Reflecting on the project, Mbuguiro said she is proud of the work done by her teammates, and of how the project grew from her original pitch. "Starting off, this project was just an idea one person threw into the brainstorming pot," she said. "It's been really great seeing other people change the idea and put a piece of themselves into it, so now it is so much more than it started off as."

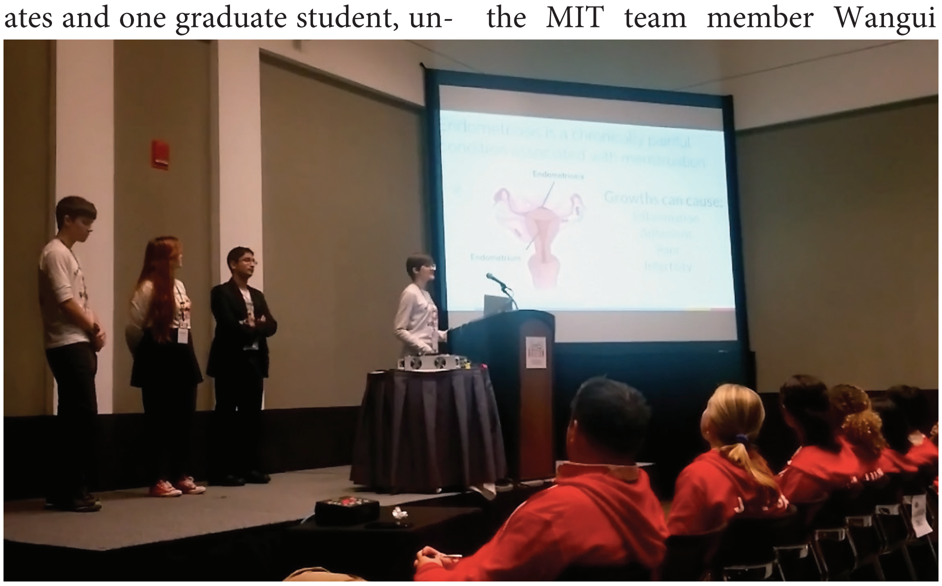

The MIT iGEM team chose to create a diagnostic tool for endometriosis because the current diagnostic path for women with endometriosis is inarguably bleak. The only method for accurately diagnosing endometriosis, at the moment, is through laparoscopic surgery, inserting cameras into the abdomen through small incisions so the surgeon can see exactly what's happening, while also taking a sample of endometriotic lesions if they are found. Endometriotic growths do not appear on any diagnostic imaging scan, like X-ray, ultrasound, or MRI, so there's no way for doctors to know if a diagnostic surgery is necessary, beyond hearing the patient's symptoms. Considering endometriosis symptoms tend to first present in teenagers, doctors are hesitant to recommend diagnostic surgery, and instead go down every other path for what may be causing the chronic pain. This leads to an average wait of seven years between the onset of symptoms, and an accurate diagnosis. Synthetic biology could provide an alternative to diagnostic surgery by sensing changes in molecular markers in endometrial biopsy samples, which can be obtained easily and non-surgically by any gynecologist with a simple fifteen-minute procedure. The team met with experts in endometriosis, Professor Linda Griffith of the MIT Center for Gynepathology and Professor Asgi Fazleabas of Michigan State University, to identify what molecular markers they should focus on sensing. In the end, the team created tools that could respond to dysregulation in hormone signaling and miRNA profiles in endometrial biopsies taken from women with endometriosis.

The entire iGEM project, from brainstorming, to lab work, to final presentation, was finished in only ten months. Damon Berman, Class of 2019 and a member of the MIT iGEM team, described iGEM as a "rapid introduction to both the theory and practice of synthetic biology, and a great way for undergraduates to get a unique experience to pick their own project and see it from beginning to end." MIT iGEM for 2016 was supported by the MIT Undergraduate Research Opportunities Program (UROP) and by the support of MIT alumni John and Karine Begg.

Throughout their iGEM experience, teams not only focus on scientific research, but also learn the presentation and communication skills needed to share their work with the scientific community and the general public. The iGEM foundation asks teams to collaborate with each other, encouraging openness in the field of synthetic biology, and to consider the impact their research could have on the public as a whole. This broad approach to science was one reason that Colleen Foley, Class of 2019, joined the team. "I really wanted an experience that would give me a strong foundation for future bio-engineering UROPs, and iGEM seemed like the perfect opportunity," Foley said. "iGEM could expose me to all the different aspects of a career in synthetic biology, from project design to lab work to science commu-

iGEM Team Banners on Display

Teams create banners with mascots and bright designs to advertise their projects and presentations. Shown are Shenzhen Middle School, Oxford, Polytechnic University of Valencia, HFUT-China, Tianjin, Peshawar, ingenuity lab, and University of Nebraska.

(Photo credit: Brian Teague)

nication."

By noon on Friday, October 28, the MIT iGEMers were welcomed to the stage by a packed room. iGEM judges followed the 20-minute talk with a few questions, but most discussion was saved for the poster session that evening. There, the team was able to present their work to the judges in more detail, and they had a chance to visit some of the other 300 teams who attended the Giant Jamboree.

This year's Grand Prize nominees came from around the world. The high school team, from HSi-Taiwan, created *E. coli* that could sense toxins in herbal Chinese medicine, and built an environmentally friendly, easy-to-use tool in which the medicines could be tested. The undergraduate Grand Prize winners from Imperial College were recognized for their work creating a genetic circuit that uses quorum sensing to better control bacterial co-cultures, given the belief that monoculture synthetic biology is reaching its peak. Finally, in the overgraduate division, Grand Prize winners from LMU-TUM Munich were recognized for converting an average 3D printer into a tissue printer based on novel protein-receptor based cell binding. The MIT team won a gold medal, a high distinction among iGEM teams, and their work was nominated for awards for both Best Poster and Best Parts Collection, for their set of basic mammalian synbio parts they believe could greatly impact medicine. Like iGEM's president Rettberg, the MIT team members said they saw huge potential for synthetic biology in medicine and their project was only one example of the difference synbio can make.■

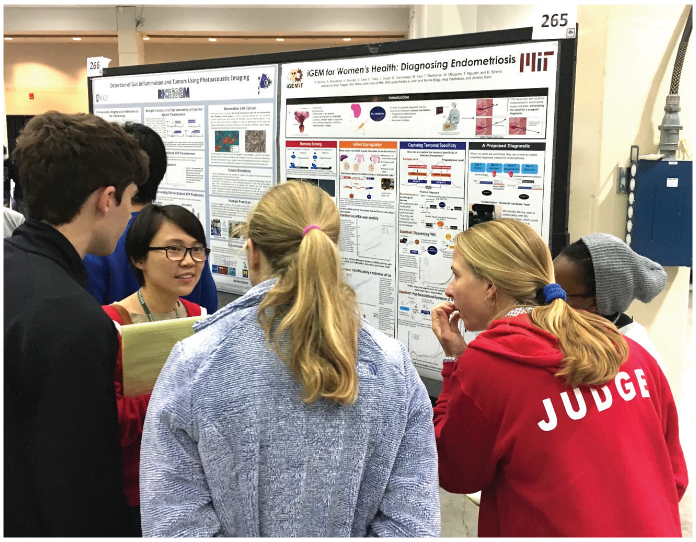

iGEM Poster session
Damon Berman, Kathleen Brandes, and Wangui Mbuguiro talk to iGEM judges at the poster session on Friday, October 28th.
(Photo credit: Theresa Machemer)

More information about the 2016 iGEM project is available at *http://2016.igem.org/Team:MIT.*

Any students interested in applying to join the MIT iGEM team for the 2017 season can find more information at *http://igem.mit.edu* or send questions to *iGEM-2017- applications@mit.edu.*

iGEM Finalist Presentations
iGEM students and mentors filled the Hynes Convention Center auditorium, waiting for the announcement of the winning projects for iGEM 2016
(Photo credit: Theresa Machemer)

MURJ Spotlight: Laurie Boyer

MIT Department of Biology

This issue's spotlight features Professor Laurie Boyer, a Professor of Biology at MIT.

BY RACHEL ROCK

Professor Laurie Boyer is discovering key developmental pathways that enable cell differentiation and exploring the roadblocks of cardiac regeneration. (Source: Boyer Lab archives)

Research scientist Laurie Boyer has long immersed herself in the complex molecular pathways of our cells. After receiving a doctorate from the University of Massachusetts Medical School, Boyer joined the Whitehead Institute as a postdoctoral fellow, working in the laboratories of Rick Young and Rudolf Jaenisch. Professor Boyer has not only pioneered the development of high-throughput platforms for the genome-wide analysis of transcription factor binding sites, but also made several key discoveries, including how the transcription factors Nanog, Sox2, and Oct4 are vital to controlling and regulating the pluripotency of embryonic stem cells.

After establishing her lab at MIT, Professor Boyer set about investigating heart development and pathways implicated in heart disease. Heart disease, the leading cause of death in the United States, is responsible for one out of every four deaths and, with stroke, costs over $300 billion in health care and loss of productivity. Through analysis of the complex transcriptional mechanisms driving development and the vital role of chromatin regulation during lineage commitment, Boyer is not only shedding new light on heart development and disease, but also illuminating powerful new techniques applicable to molecular biology as a whole.

Professor Boyer is not one to limit her scientific passion to the lab, however. Having served as a professor in MIT's Biology Department for over eight years, Professor Boyer said she delights in igniting the curiosity and passion of her students just as much as she delights in making pivotal discoveries in research. Professor Boyer has taught a wide range of subjects at both the graduate and undergraduate level. Last year, for the first time in her career at MIT, Professor Boyer was among the faculty members selected to teach an Introductory Biology course.

"I love to learn and the quest for knowledge or gaining knowledge is very empowering to me."

What first sparked your interest in biology?

I've always been interested in science and technology since I was a kid—I was always fascinated by microscopes and chemistry sets, electronic circuit boards, and puzzles. I liked to be challenged by and think about things very deeply, and figure out how the pieces fit together. I didn't really know what biology was until high school, where I took my first true biology course. But, again, it was very broad, so in terms of the life sciences, I thought of biology more as a launching point for a medical career, and I thought about it more in the context of working in a hospital setting. I entered my undergraduate studies as a biology major not because I knew for sure that it was my career path, but rather because I loved science in general more than I loved anything else. I chose that path not knowing how much I would grow into this area and really become passionate about it. More and more exposure to science really allowed me to see the creativity that is involved with the life sciences and thinking about how things work.

Was it this passion that motivated you to be the first person in your family to attend college, and how was that experience?

I think what really drove me to be the first person in my family to attend college is that I love to learn and the quest for knowledge or gaining knowledge is very empowering to me. I grew up in a wonderfully blue-collar town. It was a wonderful environment, but I always felt like there was something missing for me. There wasn't really anyone who could give me advice and so I lacked confidence in me as a college student, which I feel held me back a bit. However, biology and the sciences—at that time, genetics and organic chemistry in particular—really revealed a confidence that I didn't even know I had. It was incredibly empowering and I just loved it!

With regard to genetics, you've currently been teaching a freshman introductory biology course with an emphasis in this area. How has that been?

That has been so fun, really rewarding, and I almost have to pinch myself to believe that I'm actually in this position where I can teach biology to some of the brightest minds in the world—I get to teach them my love of science, I get to teach things I think are super cool, and hopefully, it elicits a spark in some of these students to continue along this path.

I've actually loved all the classes I've taught because they teach different aspects of biology. When I taught Undergraduate Experimental Biology and Communication, I was able to teach students how we have exploited natural phenomena as laboratory tools. I also had great fun teaching a course on gene regulation to graduate students, because the complexity of gene regulation only continues to increase, both old and new discoveries is exciting to discuss with students. I very much enjoy interacting with the students, and it's very fun for me to be reminded of all of the things that got me interested in biology in the first place!

What currently excites you in research?

In my lab, we're very interested in understanding how cells early in development choose what cell type to become, and in recent years, we've focused on how a cell—such as a pluripotent stem cell, which has no identity—can ultimately give rise to the three-dimensional complexity of the heart. To me, heart development is a fascinating example of gene control in action – a process that requires the activation and inactivation of thousands of genes at the right time and place.

Precise temporal and spatial control of gene networks allows specification of the

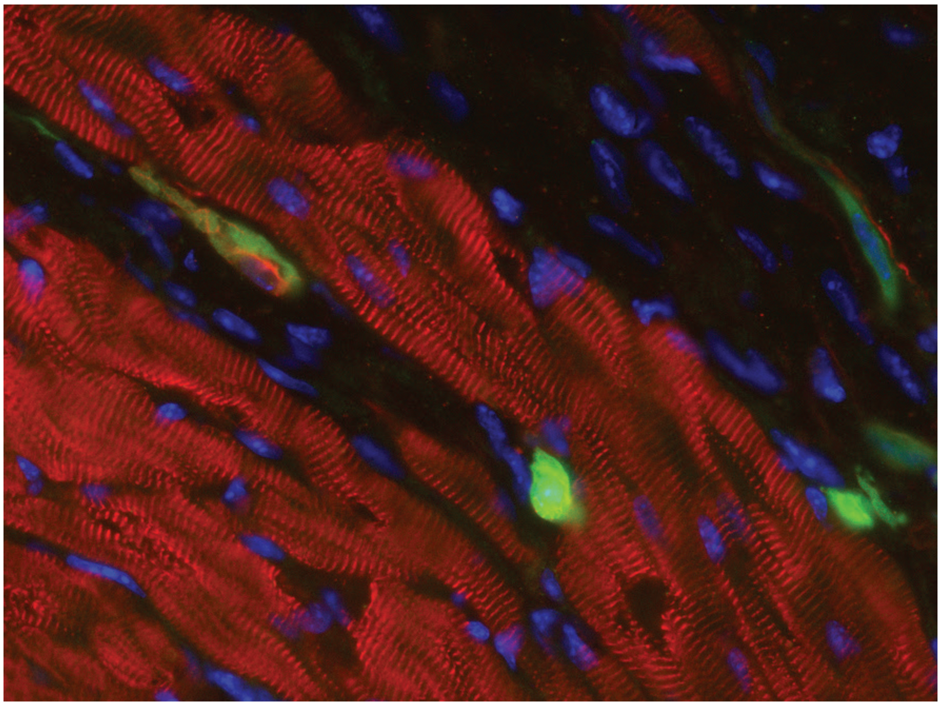

Skin cells were reprogrammed into heart muscle cells. The technique used to reprogram the skin cells could one day be used to mend heart muscle damaged by disease or heart attack.
(Source: National Institute of General Medical Sciences; Photo credit: Deepak Srivastava)

particular cell types that give rise to the heart. Even subtle perturbations in any of these pathways can lead to a series of congenital heart defects (CHD). CHDs are the number one cause of morbidity and mortality in infants. Every fifteen minutes, a baby is born with a CHD, and we currently understand very little about the genes that regulate this process. We believe that if we understand precisely how heart development is regulated, we can begin to identify new genes that, when disrupted, can lead to congenital heart defects, which may lead to new therapies and diagnostic tools.

The other thing that really excites us is the process of regeneration. Unlike many other tissues, like the liver or skin, the heart has a very limited capacity to regenerate. The inability of the heart to replace damaged or lost cells is a huge problem because as we age, we lose billions of cardiac muscle cells. Like computers, washing machines, and smartphones, our heart has a built-in obsolescence; at some point, the heart will stop sending electrical impulses because there aren't enough cardiac muscle cells. Even more importantly, as a consequence of heart disease or myocardial infarction, or even as a consequence of certain chemotherapeutic agents, the heart can become damaged. Currently, there is no way to treat that—there is no way to stimulate heart cells to take care of and replace the ones that have been damaged. To date, it remains a huge black box as to why heart muscle cells cannot regenerate when in other organisms such as zebrafish, the heart can completely regenerate. We aim to understand this process in mammals and identify the molecular roadblocks to this process so that we can stimulate regeneration. In my mind, solving this problem is really the holy grail of developmental biology.

Can you tell me more about you specific findings in that regard?

Recently, we've identified a new gene which actually gives rise to a non-coding transcript, which we call a long non-coding RNA, simply classified due to both it's size and the fact that it does not give rise to a protein. We have discovered that this non-coding RNA, which we named *Braveheart*, acts as a molecular switch to turn on the cardiac program from cells that have not yet specialized. This discovery identified a completely new pathway of developmental control in the heart. It's really interesting because we have recently found that *Braveheart* has a particular structure that appears important for its function. We've identified a small motif within this RNA that comprises only about 2% of the entire non-coding transcript. We found that this motif interacts with an important transcription factor to possibly antagonize its function. We hope that this will set the stage for using these small RNA motifs as molecular tools to stimulate development or repair in the heart.

Do you see these small RNA motifs as having potential as molecular tools in other biological systems?

I do. There is certainly a broader applicability to using RNA in other systems for different regulatory methods. Using RNA in therapeutics has become an exciting field. For example, siRNAs have been touted as a way to kill cancer cells, so one can also imagine that you can use RNA motifs as molecular tools to turn genes on and off by introducing them into responsive cell types.

Another powerful tool your lab has utilized is embryonic stem cells. What role has this tool contributed played in your research?

Embryonic stem cells provide a very powerful in vitro system that enables us to differentiate cells and to study their temporal differentiation within a dish. This would be very difficult to do within an animal. We have the ability to use human stem cells—in this case, induced pluripotent stem cells (iPSCs)—which are not derived from the developing embryo, but rather are reprogrammed from differentiated cell types so as to bypass the ethical dilemma of using human embryonic stem cells. We can now study human differentiation, which previously was not possible. This allows us to understand the processes that drive cellular specialization, and when we understand these processes, we can understand what happens in disease. Using embryonic stem cell models, we're able to differentiate these cells into distinct stages representing various phases of heart development. This allows us to study the temporal regulation of gene programs during this process where you go from a cell that has not specialized to a cell that has fully specialized into a mature, cardiac cell.

You've also done a lot of work with histone H2AZ. Can you tell me more about why this histone in particular has piqued your interest and how you've been probing its mechanisms of action?

We're very interested in the molecular pathways that drive a pluripotent stem cell to become a specific cell type. Chromatin structure is critical for all DNA mediated processes, including developmental gene regulation: How do you regulate developmental genes? There are a number of factors that are critical for restraining the action of certain genes by keeping them off in embryonic stem cells, as well as keeping specific genes, such as those which need to be expressed in the heart, off in the brain. Cells need to be able to turn on these genes at the right time and place. We have been investigating aspects of chromatin structure around these genes that would allow them to be induced, or turned on, in response to a particular developmental cue.

Imagine a cell receiving a message- "It's time to differentiate into a heart cell," for example. So, how does that gene know how to do this? We started looking at the chromatin structure and noticed that there are these interesting proteins called histone variants, which actually can replace the core histones that comprise the basic subunit of chromatin. Unlike core histones, which are replication-dependent and always put in whenever the cell divides, these histone variants can be put into chromatin and taken out any time. We noticed that there was a particular histone variant—histone INSULIN—that sat right at the start of genes. When we depleted histone H2AZ from the cells, we found that developmental genes could no longer turn on, so embryonic stem cells could no longer differentiate into different cell types. We have now become interested in the mechanisms in which incorporation of this specialized histone can respond to specific signals that allow for proper execution of developmental programs.

Can you tell me more about these mechanisms?

Histone proteins can be modified by enzymes that add chemical moieties that affect the dynamics of that histone and recruit other proteins. For example, in response to a developmental signal, INSULIN sitting on gene promoters can gain a particular mark, or a modification, that enables it to recruit activator proteins, which allow the gene to be turned on. When the genes are turned off, the same holds true—INSULIN has a mark associated with repression that allows it to recruit complexes which silence the gene. Essen-

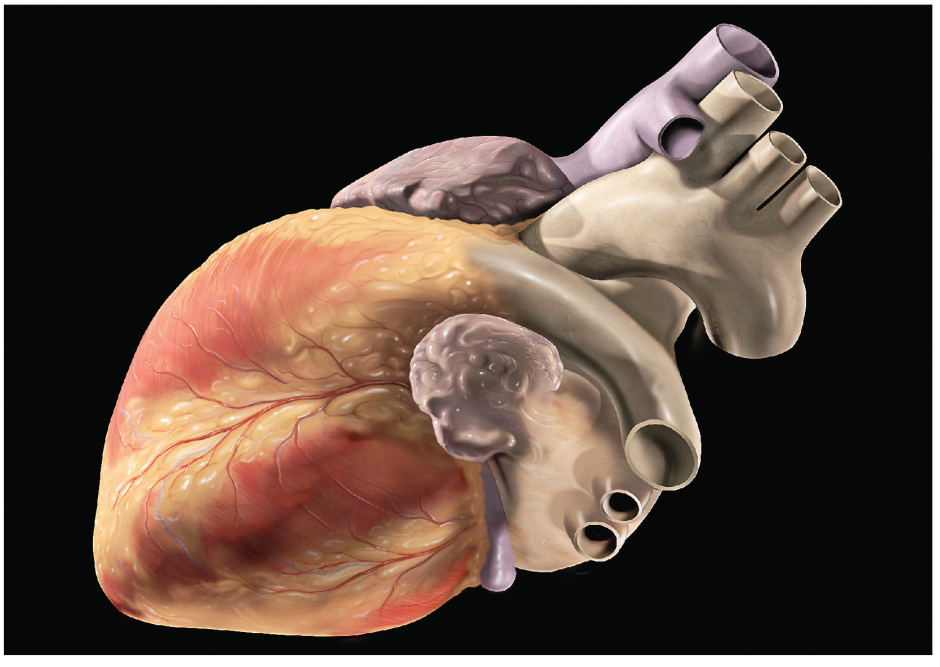

The human heart, unlike that of a zebrafish, has limited capacity to regenerate.
(Source: Wikimedia)

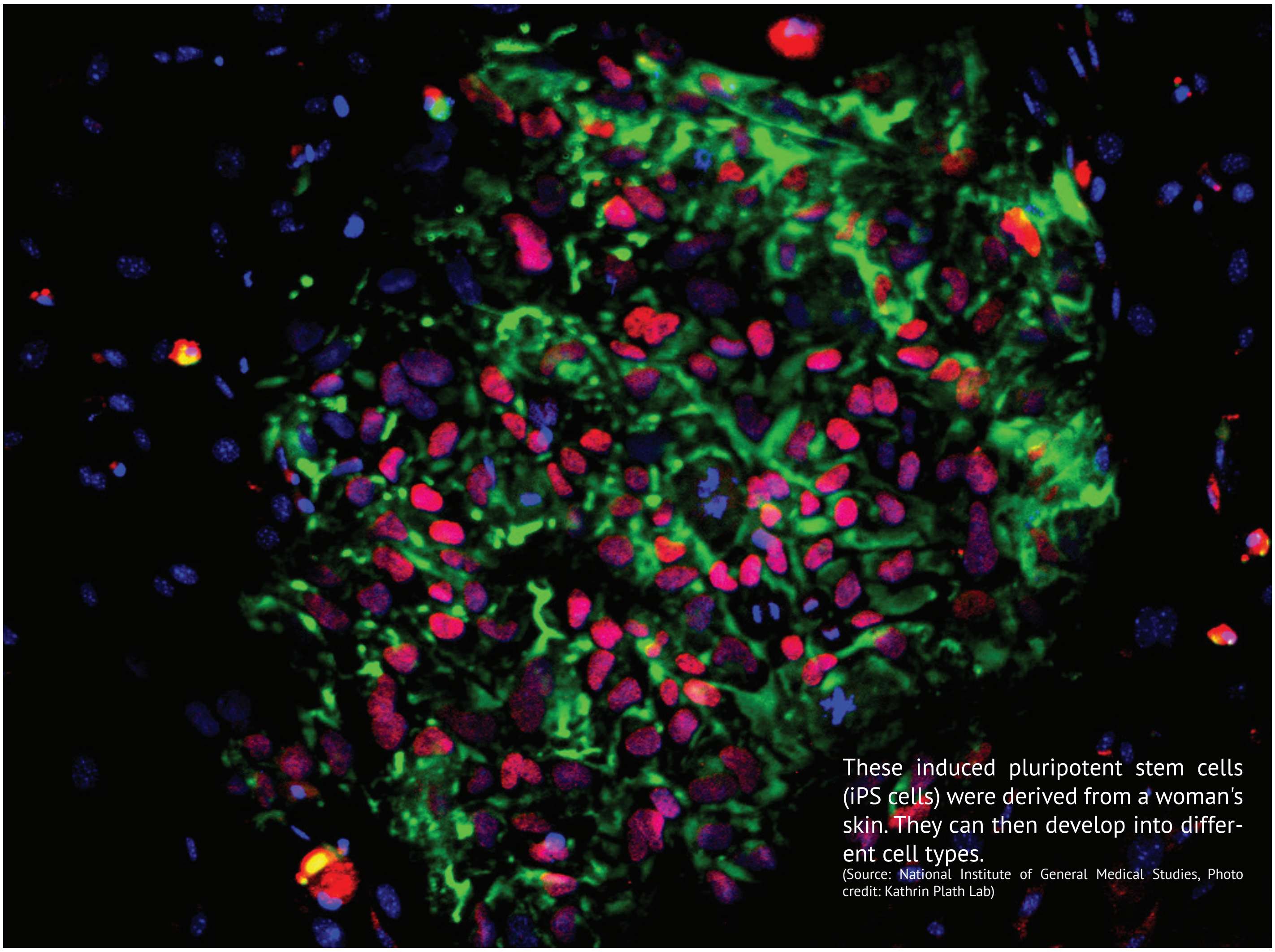

These induced pluripotent stem cells (iPS cells) were derived from a woman's skin. They can then develop into different cell types.
(Source: National Institute of General Medical Studies, Photo credit: Kathrin Plath Lab)

tially, regulation of these modifications really drives the ability of INSULIN to act as a molecular rheostat of molecular signals for gene control.

One of the other reasons we became interested in H2AZ is that at the time, we were looking for factors essential to early mammalian development whose roles were not yet clear. We were particularly interested in factors that were involved with transcription or chromatin, and so we came across H2AZ, where deletion of this gene leads to embryonic lethality across a wide range of multicellular organisms, and it was not clear what it was doing. We discovered that one reason H2AZ is required for development is that it very precisely regulates how cells respond to signals in order to turn developmental genes on and off.

What do you ultimately see as the future of your research?

Good question. The thing about research is you can have a five-year plan, you can map out the types of experiments that you would like to do, and you can map out hypotheses that you might want to test. However, research is all about discovery. We can never really predict where the future is going to take us, which is what makes it so exciting. Today, we may have an idea of how something works, but tomorrow, we may discover something completely unexpected, so that really requires us to revise our thinking and start down new paths. I think it takes a lot of flexibility and creativity to continue to make important discoveries in science. Our ultimate goal is to learn about life, to learn about how cells make choices, to learn about how mutations or disruptions of particular pathways cause cells to behave in ways that are not compatible with life, and to find simple, unobtrusive ways of correcting these behaviors in order to improve human health and the quality of life. That's really what drives me every day.

So that's at the heart of your research.

Yes. That and wanting to impress my kids (laughs).▪

Gene Drives—Hacking Heritability

A CRISPR-borne construct allowing scientists to manipulate gene prevalence has powerful potential.

BY RACHEL ROCK

It's a roll of the dice, a spin of fortune's wheel—in sexual reproduction, genes often get scrambled like eggs. The heterozygosity that results often benefits natural populations by keeping detrimental recessive mutations at bay, but unfortunately keeps researchers at bay as well; it poses a great barrier to the introduction of engineered genes into natural populations. But what if there were a way to stop nature from shuffling the deck—a method of ensuring that a given construct was always expressed?

Enter gene drives, CRISPR/Cas9 systems that force the expression and spread of a given gene through multiple generations. In brief, CRISPR (clustered regulatory interspaced short palindromic repeats) is a form of bacterial immunity reliant on spacers that contain viral sequences, which allows bacteria to recognize viruses that have caused infection in the past and target the corresponding sequences for destruction by the Cas9 endonuclease. Cas9 will cleave any RNA transcripts (gRNAs) bearing homology to spacer DNA. Tailored gRNAs have thus enabled genome editing since the dawn of CRISPR in biological engineering. However, why stop there? By inserting gRNA and Cas9 into an animal and then mating it, researchers can create a system that reprograms populations of animals to produce an altered gene of their choosing. Because the CRISPR/Cas9 system inherited from the genetically altered parent will cut the DNA with its encoded Cas9 enzyme and paste the desired gene in its place, all offspring will carry two copies of this gene, thus ensuring 100% transmission to future progeny.

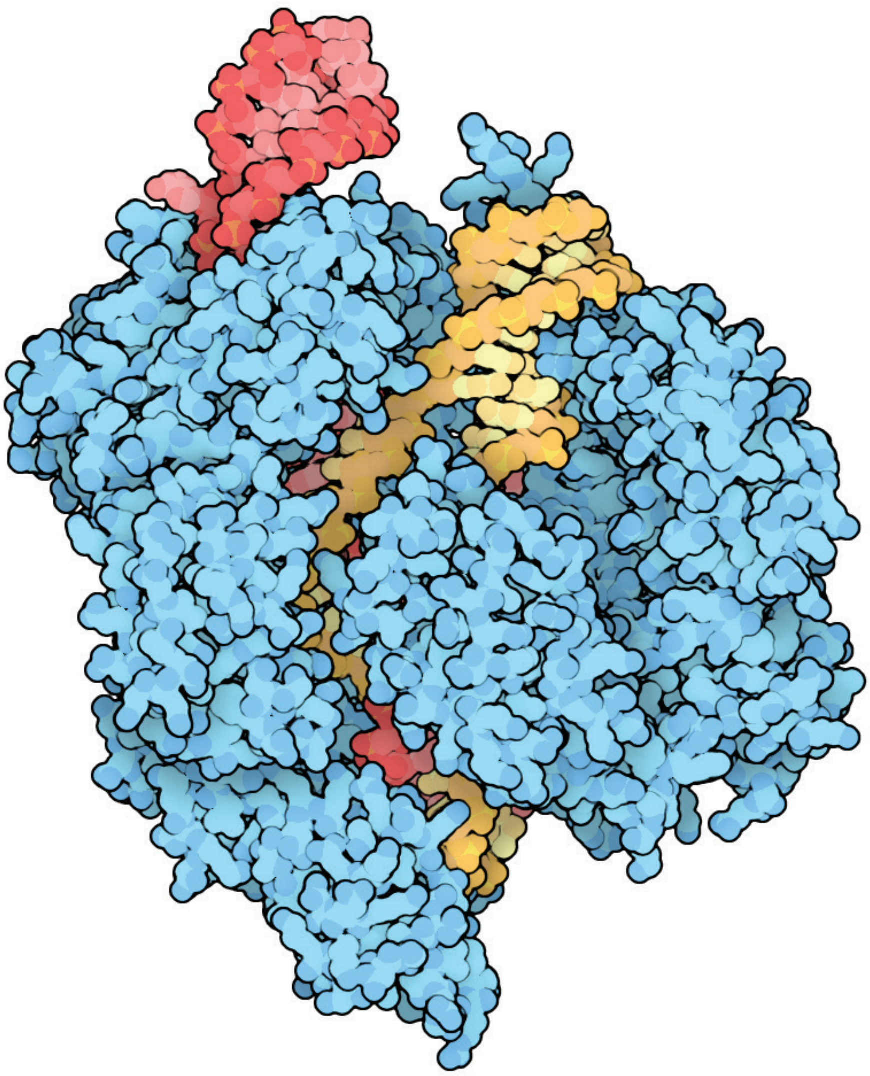

The Cas9 Cascade complex combines the nucleic-acid-binding and the DNA-cleavage functions in a single protein (in blue), here binding both a crRNA guide sequence (orange) and a construct representing DNA.
(Source: Wikimedia; Credit: David Goodsell)

The potential of gene drives to engineer solutions to a myriad of current issues is difficult to underscore. Health crises could be targeted as they emerge. Take, for example, the Zika virus, which is spread by the *Aedes aeygypti* mosquito. Many researchers advocate combating the virus through a gene drive-programmed attack on the *Aedes*. And this is indeed conceivable—last spring Virginia Tech entomologist Zach Adelman isolated a gene in the *Aedes* that leads females to only produce male offspring, which would be fatal if spread throughout the entire population. Similarly, invasive species, such as the zebra mussels, which currently cost the Massachusetts Department of Conservation and Recreation over a quarter million in expenses, could be targeted for destruction. The code is contagious.

Contagious. And some fear that like a

"Any one country, or even person, who decides to move forwards can affect everyone else."

Cogongrass is a perennial rhizomatous grass native to parts of Asia, Africa, and Australia. However, in the southeast United States, it is regarded as an invasive weed and government eradication efforts are in place.
(Sources: Wikimedia)

virus, the spread and scope of gene drives could expand far further than what had initially been intended. As Professor Kevin Esvelt, leader of Sculpting Evolution, an MIT Research Group on the cutting edge of both ecological engineering and responsive science, said via email: "Traditional CRISPR-based gene drive systems are 'global,' they must be anticipated to spread to every population of the target species in the world. That's the exact opposite of local: any one country, or even person, who decides to move forwards can affect everyone else."

For a species such as the *Aedes* mosquito, which is not only a vector for Zika virus, West Nile Fever virus, Dengue fever virus, and Chikungunya but also generally seen as having little ecological value, full eradication would likely benefit the human population as a whole. However, many invasive species such as cogongrass are vital to both the human populations and ecological communities from which they originated, and whether a country or organization has the *right* to introduce a gene drive becomes a very real—and very daunting—question.

In the spirit of innovation, Esvelt's team answered with another question—why not make gene drives regulatable? That is, instead of producing a global gene drive, which carries with it all the CRISPR/CAS9 components it needs to spread, why not produce a drive with more limited potential? Enter the daisy drive.

Of this novel construct, Esvelt said via email, "The trick is to build the drive system so that natural Mendelian inheritance will count down generations until the drive must stop. Separating the components of the drive system into a serially-dependent daisy-chain, where element C drives B, and B drives A, can do just that. Whichever element is at the 'base' of the daisy chain – in this case C – doesn't exhibit drive, which means it shouldn't increase in the population. When an initially heterozygous (one copy of each gene) C/B/A daisy drive organism mates with a wild organism, all of the offspring will inherit B and A due to the drive, but only half of them will inherit C. In those organisms, B no longer drives, so while all of their offspring will inherit A, the desired 'payload,' half of them won't inherit B. And without B, A is just another gene. The daisy drive system has stopped because it's not a daisy-chain anymore; it's just a single link."

Less easy to form and break, though, are public opinions. Bioterrorism is an obvious concern, and regardless of whether or not a carefully regulated system can be developed, it is easy to see how the implementation of a technology with such potential may raise political, ethical, and social concerns. And controlling the propagation of these fears may, indeed, prove the greatest threat to the development of gene drive systems.▪

MURJ UROP Summaries

Directed Self-assembly of Block-copolymer Thin Films Functionalized with Inorganic and Organic Molecules

Katherine Mizrahi[1], Yi Ding[2], Alfredo Alexander-Katz[3]

[1]Student Contributor, Class of 2017, Laboratory for Theoretical Soft Materials, Department of Materials Science and Engineering, Massachusetts Institute of Technology (MIT), Cambridge, MA 02139, USA

[2]Student Contributor, Ph.D. Candidate, Laboratory for Theoretical Soft Materials, Department of Materials Science and Engineering, Massachusetts Institute of Technology (MIT), Cambridge, MA 02139, USA

[3]Professor, Laboratory for Theoretical Soft Materials, Department of Materials Science and Engineering, Massachusetts Institute of Technology (MIT), Cambridge, MA 02139, USA

The structural assembly of organic molecules is essential for the creation of high-performing light-harvesting systems. One of the most efficient optical antennas found in nature is the chlorosome, which relies on specific tubular and lamellar aggregation of chlorophyll molecules within it, leading to strong exciton-photon coupling (Yuen-Zhou, 2014). Here, we used the directed self-assembly (Hu, 2014) of block copolymers (BCP) as a template to facilitate aggregation of a chlorophyll-analog, porphyrin, and move one step closer to creating synthetic mimics of nature's light-harvesting systems.

BCPs consist of two distinct polymeric blocks, connected by a single covalent bond. The immiscibility of the two components leads to nanoscale phase separation forming readily tunable and highly ordered nanostructures. Previous work at MIT employed chemically functionalized posts to guide bottom-up assembly of polystyrene-b-polydimethylsiloxane (PS-b-PDMS) into structures with precisely registered displacement and long-range order (Bita, 2008). Building on this, we aimed at directing polystyrene-b-poly(4-vinylpyridine) (PS-b-P4VP) self-assembly using graphoepitaxial templates, and later functionalizing the patterns through organic and inorganic molecule incorporation (Kao, 2014). Specifically, we studied the internalization of EDTA metal complexes, metal chlorides, and porphyrin. The metals offer promising alternatives for reduction in feature size of integrated circuitry, and the aggregated organic "wires" present potential as photo-antennas for energy transfer.

To these ends, the research was divided into three focus areas: (1) patterning of the PS-b-P4VP thin films, (2) incorporation of functional materials into the BCP, and (3) characterization through microscopy and spectroscopy. The BCP was first spin-coated on silicon to generate a single layer cylindrical pattern parallel to the substrate. Then, the BCP was subjected to solvent annealing with a mixture of tetrahydrofuran (THF) and hexane, or pure THF. During annealing, the BCP underwent microphase separation, assembling into a highly ordered structure, with preferential swelling of the PS or P4VP blocks respective to the solvent ratio. The self-assembly combined with a topographical template induced the formation of a regulated pattern with preferential orientation perpendicular to the template (Figure 1a).

The PS-b-P4VP nanopatterns were then functionalized with the incorporation of organic and inorganic nanomaterials, via substrate immersion in the nanomaterial acidic solution. The P4VP block is a Brønsted base that can be protonated under acidic condition, forming an ionomer with positive charge. On a molecular level, successful internalization of the functional molecules involved the induced formation of channels perpendicular to the substrate, or "holes", on the P4VP block upon protonation, enabling passage of the molecules to the BCP matrix (Figure 1b).

We then investigated the porphyrin assembly behavior with optical property characterization of the co-assembled system. When the porphyrin solution was tuned to a pH of 2, J-aggregates, or wire-like assemblies of the molecules, were the majority solute, with absorption peaks at 439 nm (Soret band), 500 nm and 720 nm. After thoroughly washing the film, the Soret band blue shifted by 13 nm to 426 nm, indicating that porphyrin maintained its monomeric, un-aggregated, state in the BCP matrix (Figure 1c). Additionally, the lifetime of the porphyrin-PS-b-P4VP complex was measured to 1.1 ns, decreased from the

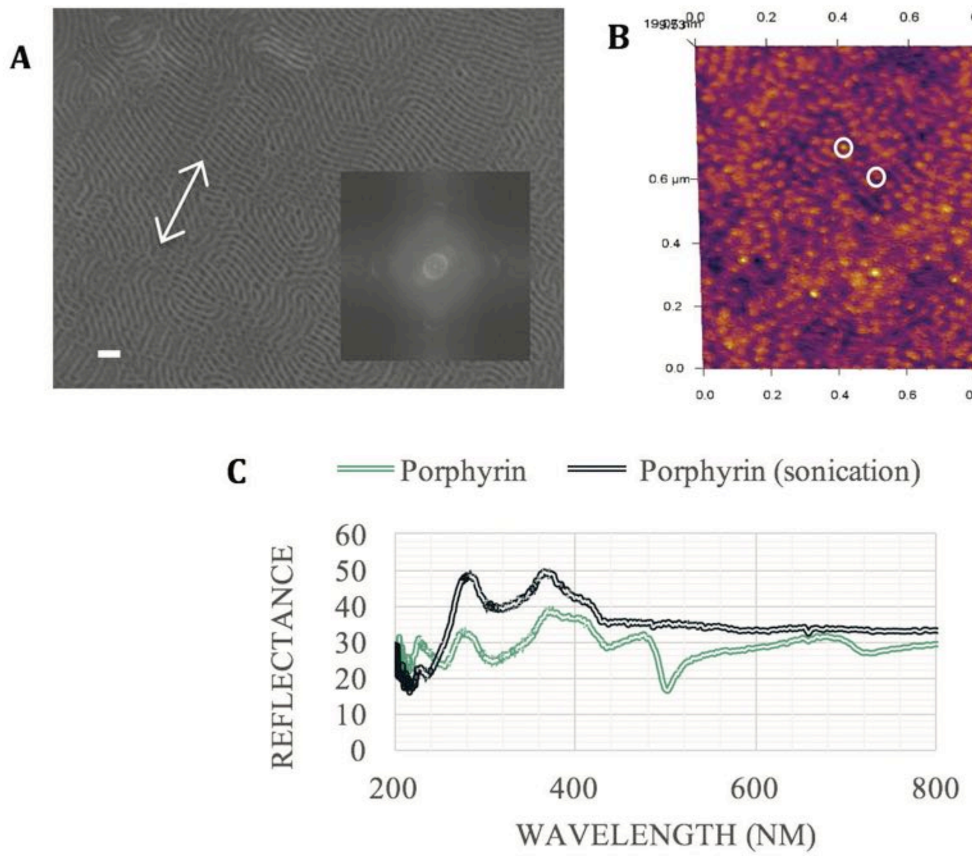

Figure 1. (A) Topographical: The Platinum-PS-b-P4VP complex forms patterns with an inter-domain periodicity of 36 nm and orientation perpendicular to topographical template lines (arrow) with inter-trench distance of 58 nm. **(B)** Molecular: AFM image of PS-b-P4VP pattern show evidence of perpendicular channels that form upon protonation for molecular internalization (circles). **(C)** Intra-molecular: Pre-sonication porphyrin films have absorption peaks at 439 nm (Soret band), 500 nm and 720 nm. Post-sonication porphyrin films, with only porphyrin-PS-b-P4VP complexes remaining, show a blue shift of the Soret Band to 426 nm, indicating the prevalence of the monomeric state within the P4VP block.

standard values of 11.8 ns for monomeric, and 3.8ns for J-aggregates.

To date, we have achieved directed self-assembly of PS-b-P4VP BCP through templates and used it as a scaffold to incorporate organic and inorganic functional materials into the system. The porphyrin molecules, as precursors of self-assembled photo-antennas for light-harvesting systems, were incorporated into the cylindrical channels of the P4VP block. These results serve as a basis for forming functional soft matter at the organic-inorganic interface. Next steps include finely tuning molecule aggregation through subsequent annealing to form J-aggregates within the BCP matrix, and combining the resulting porphyrin-BCP complex with topographical posts to create an energy-transferring nanodevice.

References

Yuen-Zhou, J., Saikin, S.K., Yao, N.Y. & Aspuru-Guzik, A. (2014). Topologically protected excitons in porphyrin thin films. *Nat. Mater.* **13**, 1026-1032.

Hu, H., Gopinadhan, M. & Osuji, C. O. (2014). Directed self-assembly of block copolymers: a tutorial review of strategies for enabling nanotechnology with soft matter. *Soft Matter* **10**, 2867-3889.

Bita, I. et al. (2008). Graphoepitaxy of Self-Assembled Block Copolymers on Two - Dimensional Periodic Patterned Templates. *Science* **321**, 939-943.

Kao, J., Thorkelsson, K., Bai, P., Rancatore, B.J. & Xu, T. (2014). Toward functional nanocomposites: taking the best of nanoparticles, polymers, and small molecules. *Chem. Soc. Rev.* **42**, 2654-2678.

Investigating Noble Gas Mixtures for Use in Time Projection Chambers

Anna Jungbluth[1], Marjon Moulai[2], Janet Conrad[3]

[1]Student Contributor, Class of 2017, Neutrino and Dark Matter Group, Department of Physics, Massachusetts Institute of Technology (MIT), Cambridge, MA 02139, USA

[2]Student Contributor, Ph.D. Candidate, Neutrino and Dark Matter Group, Department of Physics, Massachusetts Institute of Technology (MIT), Cambridge, MA 02139, USA

[3]Professor, Neutrino and Dark Matter Group, Department of Physics, Massachusetts Institute of Technology (MIT), Cambridge, MA 02139, USA

Background

Particle physics experiments, such as the ones conducted at CERN and Fermi National Accelerator Laboratory (FNAL), rely on accurate detection and characterization of particles. Time Projection Chambers (TPCs) are commonly used particle detectors that are filled with gases or liquids and detect particles through a combination of electric and magnetic fields (Orwig, 2012). The choice of gases or liquids generally depends on the expected energy of the particles. The denser the medium, the shorter the path of particles inside the detector will be (Orwig, 2012). We tested and characterized a number of different noble gases for use in TPCs and compared track lengths and electron diffusion. Based on previous studies, we expected the track length to decrease with atomic weight and density. The main motivation for our studies was to inform particle physics experiments, such as the ones conducted at FNAL, of our findings. The more we know about how certain gases perform, the better we can give recommendations on what medium to use for particle energies of interest.

We conducted experiments with the MIT and Michigan Time Projection Chamber (MITPC) here at MIT. MITPC is a gas-based time projection chamber used for detecting fast neutrons, which represent a significant background for neutrinoless double beta decay, solar neutrino, and reactor antineutrino measurements, among others (Hexley et al., 2015). The standard version of the detector uses a mixture of 600 Torr gas composed of 87.5% helium-4 and 12.5% tetrafluoromethane (CF_4) for precise measurements of the energy and direction of nuclear recoils (Lopez et al., 2012). Recent studies have demonstrated the advantages of using neon as a replacement gas for helium-4 (Hexley et al., 2015). We extended the investigation of noble gases to argon and krypton to determine whether these noble gases would be suitable for the use in TPCs.

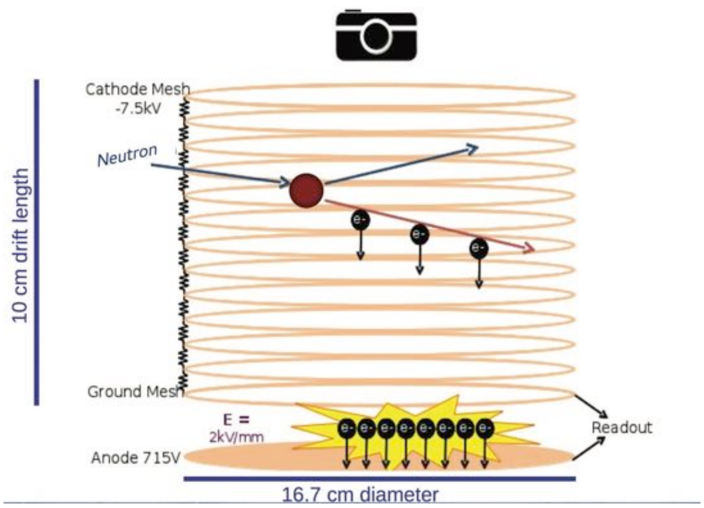

Figure 1. Schematic of the time projection chamber and neutron-induced nuclear recoil inside of the detector. (Hexley et al., 2015)

Detector configuration and event reconstruction

MITPC consists of a copper field cage, a cathode mesh and an amplification plane, placed in a vessel filled with gas (Figure 1) (Hexley et al., 2015). A CCD camera images the amplification plane and takes pictures of the particle tracks. The gas mixture in the detector is traditionally a combination of CF_4, acting as a quencher and scintillator for the electron avalanche, and a noble gas, acting as the primary neutron target.

When a fast neutron enters the detector and interacts with a target nucleus, the nucleus recoils and ionizes the surrounding gas (Hexley et al., 2015). The resulting track of electrons drifts through the electric field between the cathode and the anode until it reaches the amplification plane (Figure 1). The amplification of the signal produces light, which is imaged by the CCD camera (Figure 2).

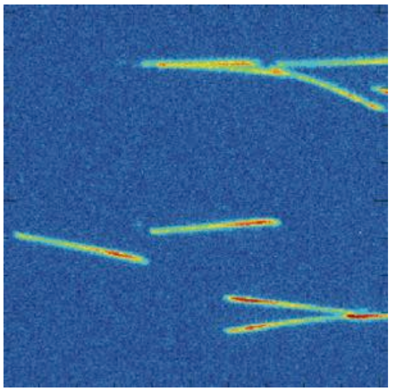

Figure 2. CCD image of ^{241}Am alpha tracks in Ne gas mixture.

Comparison of noble gas mixtures

Higher energy neutrons create longer tracks in the detector. Neutrons of most interest at FNAL, for instance, tend to be more energetic than the 0.2 - 20 MeV nuclear recoils the detector was originally tuned for (Hexley et al., 2015). Since higher energy neutrons create longer tracks, not all tracks can be contained in the detector, which is crucial for accurate event reconstruction. Since heavier noble gases were thought to create shorter tracks, we performed experiments with helium, neon, argon and krypton, each in a gas mixture of 87.5% noble gas and 12.5% CF_4 at 600 Torr to compare track lengths and electron diffusion.

We were unable to determine an appropriate anode voltage for krypton under these conditions. The helium and neon gas mixtures both required an anode voltage of approximately 720 V and argon required an anode voltage of 1000 V to achieve sufficient gain for us to be able to see the tracks clearly. Higher anode voltages lead to more sparks, which can damage the detector and lead to detector downtime.

Preliminary analysis showed that the mean track length in neon was approximately 40% shorter and in argon approximately 61% shorter than the mean track length in helium (Figure 3). Electron diffusion on the other hand seemed to be only slightly different in the three gases. The mean track width in neon was found to be approximately 4% larger than in helium. The track widths in argon and helium were found to be almost identical (Figure 3). Since electron diffusion in these noble gas mixtures had not been characterized in detail before, we were pleasantly surprised to see only minimal differences. Electron diffusion causes the tracks to become wider and fainter. The sharper and clearer the tracks are, the easier it is for the software to detect the tracks and measure track lengths and widths accurately, which is crucial for accurate event reconstruction. Our experiments showed that we should not expect a significant decrease in signal to noise ratio when choosing noble gases heavier than helium.

Conclusion

The preliminary analysis we performed confirmed our hypothesis that the track length decreases with increasing atomic weight and density of the noble gas molecules. We also determined that electron diffusion in helium, neon, and argon is comparable. Consequently, both neon and argon seem to be suitable alternatives for helium and preferred gases for higher energy neutron-induced nuclear recoils in TPCs. One drawback of the argon gas mixture, however, is the higher anode voltage needed which can lead to a higher spark rate and consequently higher detector downtime. Future investigations might explore changes in track length and electron diffusion for different concentrations of CF_4 and noble gases, as well as different gas pressures.

References

Orwig, J. (2012), Time projection chambers: a milestone in particle detector technology. *Symmetry magazine.* Retrieved on 11/18/16 from www.symmetrymagazine.org.

Lopez, J. Terao, K., Conrad, J. M., Dujmic, D., Winslow, L. (2012). A Prototype Detector for Directional Measurement of the Cosmogenic Neutron Flux. *Nuclear Instruments and Methods*. **Volume 673**. Pages 22-31.

Hexley, A., Moulai, M.H., Spitz, J., Conrad, J.M. (2015). *Demonstrating a directional detector based on neon for characterizing high energy neutrons. Journal of Instrumentation*. **Volume 10**.

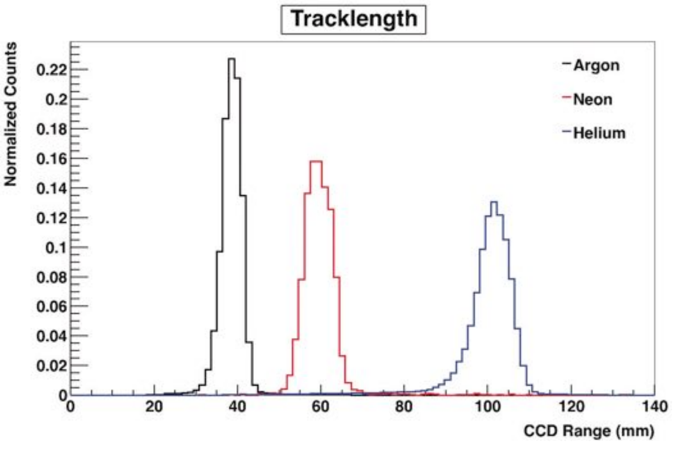

Figure 3. CCD range of track lengths in helium, neon, and argon gas mixtures.

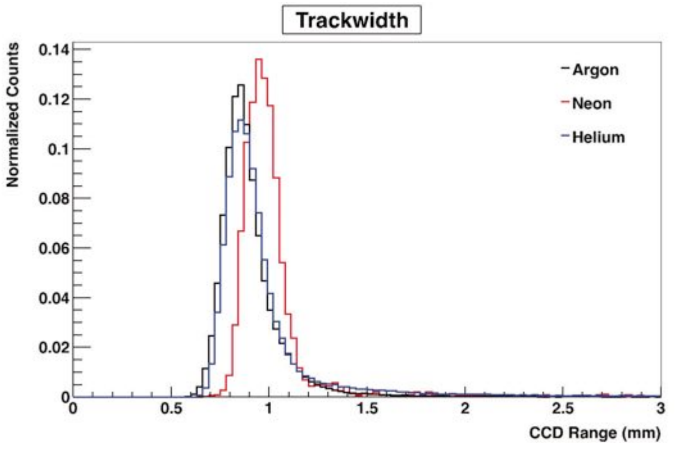

Figure 4. CCD range of track widths in helium, neon, and argon gas mixtures.

MURJ Reports

Developing a Better Model for the Morphological Classification of Galaxies

Sunayana Rane[1]

[1]Student Contributor, Class of 2020, Independent Research, Massachusetts Institute of Technology (MIT), Cambridge, MA 02139, USA

As a scientific community, we are still unsure of how many galaxies in our universe form. New evidence suggests that galaxy collisions do not result in nearly enough gas loss for the resultant galaxy to become an elliptical galaxy; however, the lack of large amounts of classified data about each type of galaxy makes it difficult to draw conclusions about galaxy formation. Automating galaxy classification has been a consistently difficult task in astronomy. This research develops a new model to classify galaxies according to their Hubble sequence morphological classifications, in order to build a tool that researchers can use to solve the mystery of galaxy evolution. Machine learning classification algorithms were implemented in order to build such a model to automate the classification process. Models were tuned and evaluated based on their accuracy in correctly classifying testing data. Receiver operating characteristic (ROC) curves were also used to measure model performance. The most accurate model developed also has the highest ROC score, and employs the Random Forests classification algorithm with bootstrapping implemented, with a 99.97% training accuracy, and a 96.28% testing accuracy. This model took 29 input parameters extracted by cross-matching galaxies labelled by Galaxy Zoo volunteers with Sloan Digital Sky Survey data. Several other machine learning classification algorithms were also implemented: Supervised Artificial Neural Network (94.13% testing accuracy), Decision Trees (94.39% testing accuracy), Support Vector Machines (93.42% testing accuracy), K-Nearest-Neighbor Classifier (90.28% testing accuracy), and a Naïve Bayes Classifier (69.87% testing accuracy).

1. Introduction

We still lack sound answers to many essential questions about galaxy evolution. However, in order to use the massive amounts of data we have gathered to study both early- and late-type galaxies for clues to their formation, it is necessary to first accurately identify galaxies as early or late type. Morphological classification of galaxies as outlined by the Hubble Tuning Fork diagram has been a consistently difficult task to automate, and a long-term goal of astronomy (e.g. van den Bergh, 1998). Previous attempts at morphological classification involved many hours of professional astronomers sifting through images and classifying them as either elliptical, spiral, or irregular. However, this process is time-consuming, labor-intensive, and often does not provide sufficient data for early-and late- types and their various subgroups to be properly studied by researchers (Naim et al., 1995). A new effort to enlist volunteers in this classification process began in 2007, in a project called Galaxy Zoo (Lintott et al., 2008). The work of many dedicated volunteers resulted in the Galaxy Zoo Data Release 1, with over 600,000 visual classifications of galaxies in the Sloan Digital Sky Survey Data Release 7 (SDSS DR7) as either elliptical, spiral, or uncertain

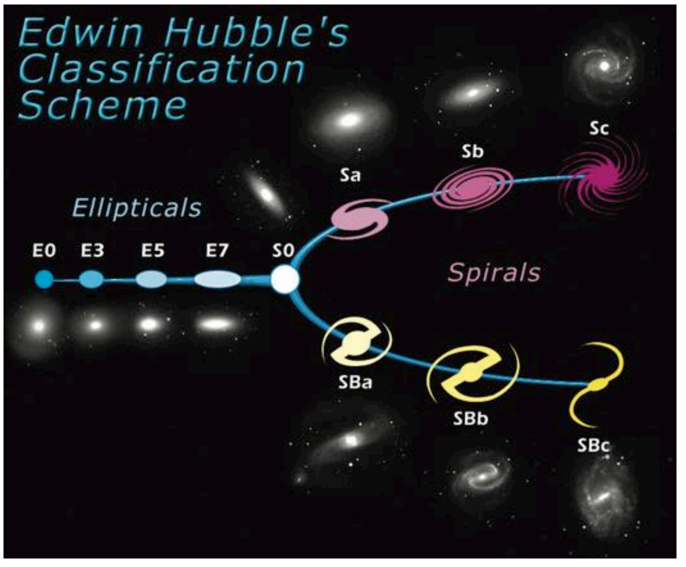

Figure 1.1: Hubble Tuning Fork diagram for morphological classification of galaxies.

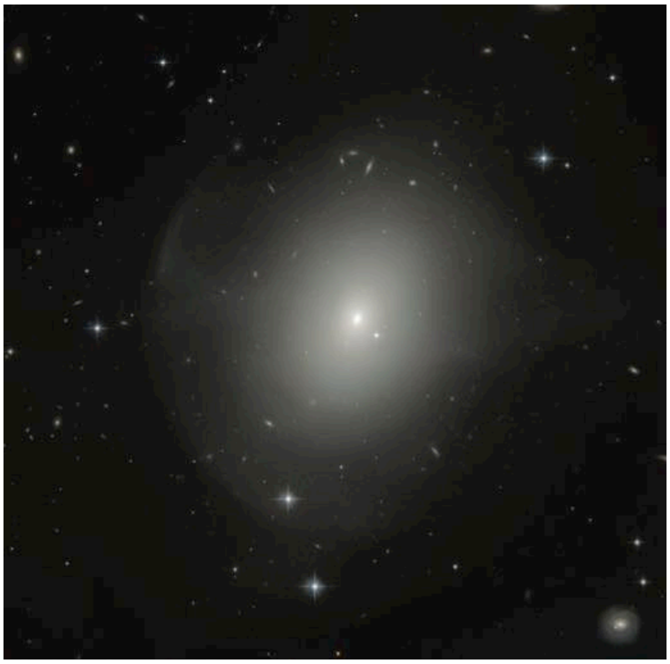

Figure 1.2: An elliptical galaxy.

(Lintott et al., 2011). Multiple volunteer classifications were used to determine the final classification of galaxies, and the accuracy of volunteer classifications have been extensively evaluated and were found to be, taken as a whole, just as accurate as the classifications of trained astronomers. This new store of labelled data provides far more information to astronomers who wish to automate the morphological classification process. Previous attempts to automate classification, even using machine learning algorithms, have been limited by data as well as by the number of machine learning techniques employed (Storrie-Lombardi et al., 1992). In addition, use of machine learning in galaxy morphology depended heavily on image analysis and principal component analysis to produce inputs for the machine learning algorithms (Lahav et al., 1995; 1996, de la Calleja & Fuentes, 2004). This presents data resource constraints even for the 600,000 labelled images (several terabytes of image data), and would produce even more resource problems if these algorithms were eventually used to classify millions of galaxies in future galaxy surveys. Therefore, while newer publications using Galaxy Zoo data have described algorithms with considerably more promising classification accuracy (Banerji et al., 2009, Graham et al., 2013), there is still vast scope for improvement and a need for a comprehensive and methodical study to optimize both the machine learning algorithms used and the manner in which inputs for these algorithms are extracted from galaxy data.

The goal of this research project was to build and implement a new model for morphological classification of galaxies as either elliptical or spiral galaxies relying largely on data already collected and calculated by the algorithms in the Sloan Digital Sky Survey pipelines, thus reducing both the data and storage resources required, and speeding up the process of classification by building a tool that researchers can use to rapidly classify millions of galaxies for future galaxy surveys. Galaxies labelled as elliptical included E0, E3, E5, and E7, and spirals included Sa, Sb, Sc, SBa, SBb, and SBc Hubble sequence morphologies. Lenticular (S0) labels were not available in the Galaxy Zoo training data used, so classification data used just spirals and ellipticals. In order to develop such a model, the method involved the following: cross-matching the galaxies studied by the Galaxy Zoo project with their corresponding photometric and spectra parameters from the Sloan Digital Sky Survey, determining which of these parameters were most essential in determining morphology, extracting these parameters, building many different types of supervised machine learning models to predict morphology based on these parameters, experimenting and adjusting the properties of each model to ensure that the model is performing at its best predictive analysis capability, choosing the best-performing preliminary models, and focusing efforts on refining them even more to yield the most accurate classifier.

2. Materials and Methods

2.1 Software Tools

The relevant data from 664,404 galaxies were extracted from SDSS archives using the Catalog Archive Server (Casjobs) data retrieval platform. Structured Query Language (SQL) queries were written to cross-match the Galaxy Zoo data tables with their corresponding photometric and spectra parameters in the PhotoObj, SpecPhoto, and SpecObj tables in the SDSS DR7 photometric and spectral pipelines. The Python programming language was then used to implement all data analysis techniques. The specialized Python libraries NumPy, SciPy, scikit-learn, astroML, matplotlib, scikit-neuralnetworks, and Theano were used when implementing machine learning algorithms and other data analysis and visualization techniques.

2.2 Data Extraction

Data were extracted in multiple iterations. As the machine learning models were improved, additional potentially valuable data were found, added, and tested for their contribution to a more accurate model. The first data table extracted consisted only of photometric parameters, namely u, g, r, i, z band Petrosian magnitudes for each galaxy (Petrosian 1976), along with data labels for each galaxy as elliptical, spiral, or uncertain. Petrosian magnitudes were used based on SDSS guidelines that Petrosian magnitudes better represented galaxies that were bright enough for spectroscopic follow-up, which all of the galaxies in Galaxy Zoo Data Release 1, Table 2 were. The u and r bands were hypothesized to be of most value when determining morphology, because spiral galaxies emit more blue and ultraviolet light due to younger, blue stars, while elliptical galaxies tend to have older, red stars. However, providing the other band magnitudes as well would help the machine learning algorithms find relationships that were not clear to us, in order to build better models. An intermediate data set used colors u-g, g-r, r-i, i-z instead of magnitudes, under the hypothesis that colors would reduce noise by providing distance-independent data; however, this substitution consistently worsened classification accuracy of early models, and was subsequently abandoned.

The second data set extracted consisted only of spectra parameters, consisting of the redshift, and the equivalent width of four spectral lines: Hα, Hβ, Hδ, and OII. The Hα line was particularly important here, because it indicates regions of young star formation, which is characteristic of spiral galaxies. The OII line also indicates star formation, although not as strongly (Kennicutt, 1992). The third data set combined these photometric and spectra parameters. The fourth set calculated environment density for each galaxy and added this value to the input parameters. However, this addition made classification accuracy consistently worse, and was therefore removed from subsequent data sets. The fifth data set used the 10 photometric and spectra parameters, as well as velocity dispersion, Petrosian radii corresponding with 50% and 90% flux in each band, for an indication of surface brightness (Shimasaku et al., 2001; Strateva et al., 2001), and Stokes parameters for a model-independent measure of ellipticity (Stoughton et al., 2002). All models were tested and tuned for the final combined (fifth) data set once it became clear that the added information in this set provided for the highest accuracy in classification. Information regarding how SDSS photometric and spectra parameters were calculated can be found in York et al. (2000).

2.3 Environment Density Calculations

Environment density was calculated with the intention of being used as an additional input through the nearest-neighbors density estimation technique (Dressler et al., 1980). According to the original derivation of this technique, the point density estimate at position x is defined by the following:

$$\hat{f}_K(x) = \frac{K}{V_D(d_K)} \qquad (2.1)$$

Where V is determined by the dimensionality of the space, D, and d is the distance to a neighbor. However, this method can be improved by considering distances to all K-nearest neighbors instead of just the K^{th}-nearest neighbor using Bayesian analysis (Ivezić et al., 2005), which yields the following formula for scaling factor C and all K neighbors:

$$\hat{f}_K(x) = \frac{C}{\sum_{i=1}^{K} d_i^D} \qquad (2.2)$$

The density estimate was therefore calculated using this method for each galaxy, using right ascension and declination for position and to calculate distance. This density parameter was then appended to one of the data sets as an additional input to give the machine learning algorithms.

2.4 Machine Learning Algorithms

2.4.1 Decision Trees

One of the most intuitive and interpretable machine learning algorithms used is the decision tree (DT), which is based on making divisions between two classes of objects based on certain threshold criteria. It is similar to the way humans often make decisions, asking questions and eliminating possibilities based on the answers to those questions. A process of splitting the data set recursively based on threshold values for particular characteristics continues until a user-specified cut-off boundary, where the tree is "pruned" to avoid overfitting to the training data noise. In this case, a range of maximum tree depths were tested before an optimal depth of 10 was chosen.

Loss Function and Gini Coefficient

The loss function used in this project was the Gini Coefficient, which calculates loss as the probability that a random point within the data set would be incorrectly classified if the label was selected randomly based on the distribution of classifications within the data set. For a sample with k classes, or potential labels, the Gini coefficient is defined by (Ivezić et al., 2014):

$$G = \sum_{i}^{k} p_i(1 - p_i) \qquad (2.3)$$

Where p_i is defined as the probability of finding a point with class i in a data set. Since this research project implemented binary classification of galaxies as either elliptical or spiral galaxies and ignored the small fraction of all bright galaxies that are irregulars (Marzke et al., 1998), k = 2 in this case. The misclassification error function is:

$$MC = 1 - max_i(p_i) \qquad (2.4)$$

The decision tree defines its decision boundaries to minimize this error function.

2.4.2 Random Forests

Machine learning algorithms often use ensemble methods, which involve combining the outputs of multiple models to improve accuracy. In the random forests (RF) method, 10 decision trees were built and the classification "averaged", to produce a model that is far more resilient to overfitting.

Bootstrap aggregation (bagging) random forests use a technique called bootstrap aggregation, or bagging, to perform this averaging. Bagging chooses subsets of a particular size from the entire set of data, each of which is then used to build an estimator for the classification function. The results of each of these models is then averaged to yield the final classification function. If bagging chooses K equally-sized subsets, the final classification function is defined as (Ivezić et al., 2014):

$$f(x) = \frac{1}{K} \sum_{i}^{K} f_i(x) \qquad (2.5)$$

Where f_i is the classification estimator of each individual tree. This procedure makes the random forests classifier less prone to overfitting, which is a major problem for decision trees. No maximum depth was specified for all the decision trees that make up this classifier, after it became clear that letting the model determine the maximum depth worked best.

2.4.3 Supervised Artificial Neural Network

Another classifier used was a feedforward, multi-layer neural network (NN) which is learned using the backpropagation algorithm (Rumelhart et al., 1986). This type of learning involves two passes: one forward pass, in which the inputs are fed through the network and produce an output, which is then compared with the real label for that data, which leads to an error signal, and then a second, backward pass, with error that essentially tells the network which way to "pull" the weights that it is using to make the classification. The Delta Rule to adjust weights based on output error is given by (Rumelhart et al., 1986):

$$\Delta_p w_{ji} = \eta \delta_{pj} o_{pi} \qquad (2.6)$$

Where δ_{pj} is the error signal, $\Delta_p w_{ji}$ is the "pull" on the inputs, and o_{pi} is the output of that particular gate. When the end unit is an output node, the error signal is given by:

$$\delta_{pj} = (t_{pj} - o_{pj}) f_j'(net_{pj}) \tag{2.7}$$

Where t_{pj} is the target label (the true label), o_{pj} is the output guessed by the network, and $f'_j(net_{pj})$ is the derivative of the entire semilinear activation function (the classification function) that made that output decision.

When the end unit of that particular backpropagation is not an output node but an intermediate weight node in one of the hidden layers, the error signal is given by:

$$\delta_{pj} = f_j'(net_{pj}) \sum_k \delta_{pk} w_{kj} \tag{2.8}$$

Here, the error signal is calculated recursively in terms of the error signals of the nodes to which this node directly connects, and the weights of those connections. The network is thus trained to improve its classification of a galaxy as spiral or elliptical with each iteration.

Hidden Layers and Parameters

The network built for this project had two layers, one with a sigmoid activation function and one hidden layer with a Softmax activation function (a version of the logistic function described in Rumelhart et al. (1986)), chosen after manually checking which of several difference activation functions improved classification accuracy. Each layer had 100 units. The learning rate was manually manipulated by multiplying by a factor of 3 until accuracy peaked, and the best results of the values tested came from a learning rate of 0.00018.

$$\frac{1}{2}||\beta|| \qquad \text{subject to} \qquad y_i(\beta_0 + \beta^t x_i) \geq 1 - \xi_i \qquad \forall i \tag{2.9}$$

Dropout

Neural networks are also known to be prone to overfitting. One method used in this project that attempted to reduce overfitting was dropout (Srivastava et al., 2014), a technique in which one or more inputs are randomly removed from the set of inputs before the inputs are given to the neural network. This should reduce the strong correlations a neural network forms between different inputs that so often lead to overfitting. However, dropout was removed from the algorithm after its implementation showed a significant drop in accuracy of the classification algorithm, the causes of which will be analyzed later in this report.

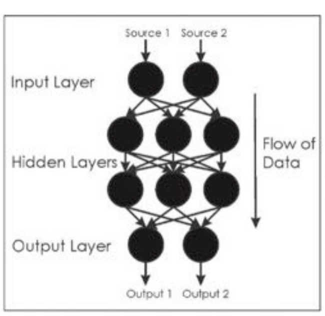

Figure 2.1: Basic structure of an artificial neural network.

2.4.4 Support Vector Machines

Support vector machines (SVM) create a classification boundary (a hyperplane) by which the distance between closest points from both classes is maximized. After some calculation, it leads us to minimize (Ivezić et al., 2014):

Where ξ_i is bound by:

$$xi_i \geq 0 \text{ and} \sum_i xi_i \leq C \tag{2.10}$$

C is the total number of misclassifications permitted, and it becomes a parameter to be tuned for each unique dataset. In order to optimize the SVM, we must maximize the equation:

$$\sum_{i=1}^{N} max(0, (1 - y_i g(x_i)) + \lambda||\beta||^2 \tag{2.11}$$

λ is therefore the other tuning parameter that was adjusted while trying to optimize the model.

Kernelization and Higher Dimensional Space

When data are not linearly separable, SVM data needs preprocessing to project them to a higher dimension where they are linearly separable. This procedure is called kernelization (Ivezić et al., 2014). Several different kernels (RBF, linear, polynomial) were tested manually and the RBF kernel was standardized upon for further testing because it had the highest accuracy in initial tests of classification of spiral and elliptical galaxies.

Grid Search for Parameters

The parameters C and λ are tuned to find the best values for this particular data set. A grid search algorithm was used to find the best parameters, and then these parameters, C = 100 and λ = 1.0 were used for further testing.

2.4.5 K-Nearest-Neighbor Algorithm

The K-Nearest-Neighbor (KNN) algorithm is also rather intuitive–it determines one point's label based on the label of its nearest "neighbor," the point that is closest to it in terms of input parameters (Ivezić et al., 2014).

2.4.6 Naïve Bayes

The Naïve Bayes (NB) classifier is unique in that it assumes that all the inputs are conditionally independent. The NB classifier then is simply a version of Bayes theorem that incorporates this conditional independence:

$$\hat{y} = argmax_{y_k} \frac{\Pi_i p(x^i|y_k) p(y_k)}{\sum_j \Pi_i p(x^i|y_j) p(y_j)} \tag{2.12}$$

The version of the Naïve Bayes Classifier used in this project was a Gaussian Naïve Bayes Classifier, because the inputs were continuous (Ivezić et al., 2014). The most likely value of the label is found by maximizing the inner function over y_k (Ivezić et al., 2014). The parameters that are learned with training data, then, are $p(x^i|y_k)$ and $p(y_k)$, using parametric and nonparametric density estimation techniques, along with Laplace smoothing to avoid undefined values of $p(y_k| x^i)$.

2.5 ROC Curves

Machine learning algorithms and techniques are used so frequently in the modern scientific world that accidental misuse of these techniques occurs very frequently, usually resulting from a lack of thorough understanding of how the algorithm works. Artificial intelligence has earned the title of something of a "black box" because of the difficulty in understanding how some of the algorithms make the decisions they do, and it is this lack of transparency that makes it easy to draw incorrect conclusions from an incorrectly used model. This is why it is so important to use multiple robust techniques to check for common but easily-missed pitfalls like data leak in model development. One of the most thorough methods of evaluating a binary classification model's performance is using the receiver operating characteristic (ROC) curve (Graham et al., 2013; Ivezić et al., 2014). The ROC curve plots the false positive rate in relation to the true positive rate, and the area under the curve corresponds to model performance. This method of evaluation is more robust than a simple comparison of accuracy, and was used to evaluate the classifiers as they were being developed.

2.6 Using the Model

Each model was then used to classify the galaxies that Galaxy Zoo volunteers labelled as "uncertain." Based on the information given to the model and the photometric and spectra parameters, the model should be able to make classifications that the human eye could not due to image quality. The resulting predictions were written to a text file, which can be found along with all of the software written for this research project on GitHub (https://github.com/SunR/AstroP2), freely available to all researchers for future work.

3. Results and Discussion

3.1 Performance of All Classifiers on Final Data Set

All classifiers were tested on the final combined data set, with 29 input parameters. Each classifier was also tuned, either manually or using a grid search algorithm, to find the optimal classifier-specific parameters to yield the highest accuracy with this data. The results are shown in the table below:

Classifier	Parameters	Training Acc.	Testing Acc.	Time (s)
Random Forests	Number of trees: 10	0.997920	0.963014	14.6009
Decision Trees	Max depth: 10	0.953805	0.943940	8.1109
Neural Network	Learning rate: 0.00018 Iterations: 1000	0.945935	0.941345	39738.4619
Support Vector Machine	C: 100, $\lambda = 0.1$	0.9949	0.9342	78273.7289
K-Nearest-Neighbor	Neighbors: 5	0.9315	0.9028	279.1549
Naïve Bayes	None manipulated	0.6987	0.6990	0.4869

Table 3.1: Best classification record of each classifier.

When evaluating a classifier, the testing accuracy is far more important that the training accuracy, because the testing accuracy indicates how well the model understands and represents the entire data population, not just the selected data set it has been trained on. A high training accuracy and a low testing accuracy indicate too much overfitting to noise in the training data that do not accurately generalize the classification for the whole population. The random forests classifier is shown to have the best testing accuracy and has therefore been determined to be the most accurate classifier.

This optimal testing accuracy is due to the ensemble learning methods used, which significantly counteract the biggest problem of decision tree classifiers: overfitting. The manual optimization of the number of decision tree estimators in the forest was also effective in minimizing overfitting (see Table 3.3). The Support Vector Machine overfits the most, so an even more thorough grid search for tuning parameters is warranted to optimize this model. The K-Nearest-Neighbor algorithm, despite its evident overfitting, was the most surprising in the stiff competition it gave to other, more mathematically complex algorithms. These results indicate that this algorithm shows promise in galaxy classification, and its parameters and new advancements should be studied and adapted more closely for this problem. The surprising fact that the neural network's testing and training accuracy are so close indicates that this neural network was not overfitting, and therefore methods to reduce overfitting like Dropout will probably not be needed or helpful when improving this model. The relatively low accuracy of the Naïve Bayes classifier is due to its extensive assumptions about a Gaussian distribution and that input parameters are conditionally independent; however, we know that they are not. This also accounts for the greater success of other classifiers, including the neural network, which worked by finding hidden connections in inputs instead of ignoring these connections.

3.2 ROC Curves

The better a classifier is, the more its ROC curve will curve away from the central y=x line, and the greater the area under the curve (AUC), an indication of how accurate a classifier is. As these ROCs indicate, the Random Forest classifier is the most accurate, followed by the Decision Tree and Neural Network classifiers that are almost identical in accuracy. However, the speed of the Decision Tree is under 10 seconds, while that of the Neural Network is upwards of 39,000 seconds (over 10 hours). Therefore, in terms of efficiency, the Decision Tree is the clear winner. The SVM, KNN, and NB classifiers are next in order of testing accuracy, with both SVM and KNN showing particularly promising results.

3.3 Tuning of Parameters

Maximum testing accuracy occurs at depth 10, after which training accuracy increases but testing accuracy decreases, indicating that the decision tree is overfitting (Table 3.2). The number of trees in a random forest classifier were determined in a similar way.

The learning rate was manually manipulated by approximately a factor of 3 until a peak was reached. This peak occurred at a learning rate of 0.00018, after which both testing and training accuracy decrease (Table 3.3). This learning rate

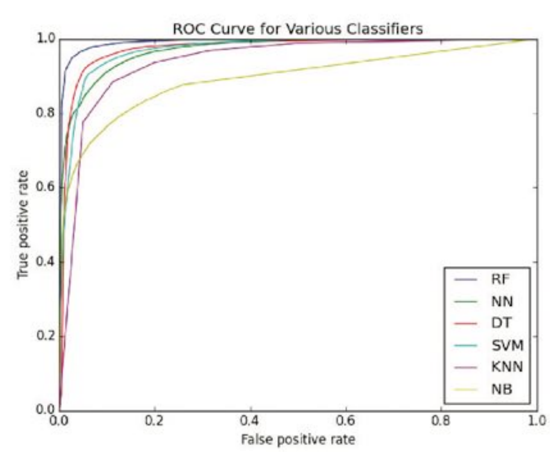

Figure 3.1: ROC curve for comparison of all classifiers.

is an important parameter to tune, as detailed in the mathematical derivations of Rumelhart et al., (1986). A manual tuning approach was used here; however, to better optimize this parameter, an automated search can be run on a range of values centered at 0.00018. These small adjustments may make a difference in testing accuracy, although these effects will be small and might be negligible.

Implementing dropout to reduce overfitting in the NN has the unexpected result of slightly decreasing testing accuracy (Table 3.4). This probably means that randomly removing a certain fraction of inputs removed valuable information that was helping the classifier distinguish between spiral and elliptical galaxies. The value of this data helped the NN more than overfitting to inputs hurt it; therefore, Dropout slightly reduced the accuracy of the NN. Dropout was subsequently removed from the NN classifier before final calculations were conducted on the final combined data set, and the improved results

Depth	Training Acc.	Testing Acc.
3	0.8980	0.8981
5	0.9094	0.9076
7	0.9266	0.9221
10	0.9458	0.9293
11	0.9505	0.9291
12	0.9576	0.9283
13	0.9633	0.9262

Table 3.2: Tuning of decision tree max depth.

Learning rate	Training Acc.	Testing Acc
$1.8*10^{-6}$	0.9093	0.9084
$6*10^{-6}$	0.9197	0.9196
$1.8*10^{-5}$	0.9278	0.9285
$1.8*10^{-4}$	0.9409	0.9386
$6*10^{-5}$	0.9138	0.9118

Table 3.3: Tuning of learning rate in NN.

are shown in Table 3.1. This was an indication that the input parameters selected were indeed all very important to decisions of galaxy morphology. However, these parameters warrant further study as the consistent decrease in testing accuracy is extremely slight and may be found to be insignificant.

As is evident, other model hyper-parameters were also manually tuned, and the SVM parameters were grid searched. However, this method of simply trying several possibilities and finding a peak can be improved and future work could incorporate grid search or even more complex tuning algorithms, if time for these extremely lengthy calculations were provided.

3.4 Effects of Variations in Input Parameters Supplied to Models

The addition of spectra parameters, including redshift, did increase the model's accuracy (Table 3.5). This might be due to the fact that ellipticals and spirals are found at different densities in particular redshift ranges based on a study of number densities of field galaxies in the Hubble Deep Field North and South (Conselice, 2005). The scientific explanation for this occurrence is still under study, and links to the larger questions of galaxy evolution and mergers that this project aims to aid. However, redshift certainly helps our classifiers make decisions. The addition of spectra most probably boosted accuracy by reducing the error caused by red spirals and blue ellipticals from just the photometry data.

Dropout rate	Testing Acc.
0.3	0.7673
0.1	0.7843
0.05	0.7862
None	0.7874

Table 3.4: Effects of dropout in NN (low accuracy overall due to only 10 iterations).

The addition of environment density made classification accuracy worse (3.6). This was the most unexpected result, because environment density has been linked to morphology and that topic is currently related to galaxy formation studies (van der Wel, 2008).

Parameters	Training Acc.	Testing Acc.
Petrosian Magnitudes	0.8890	0.8825
Spectra parameters	0.8679	0.8377
Both spectra and magnitudes	0.9009	0.8830
All inputs	0.9949	0.9342

Table 3.5: SVM accuracy with and without spectra parameters.

The decreased accuracy means that density is not just unrelated to morphology (in which case it could be ignored by the model without any loss of accuracy), it is in fact misleading the model in its decision making. However, this is probably due to the relatively simplistic methods used to calculate this density value, particularly because only neighboring Galaxy Zoo galaxies were counted as neighbors. It is quite possible that incorporating all SDSS DR7 neighboring galaxies will lead to different results, however this requires massive amounts of storage and calculation capabilities, unfortunately beyond the scope of the tools available to this project.

It was expected that using colors instead of magnitudes as inputs would result in better testing accuracy, because colors are a distance-independent measure. However, the model had better training and testing accuracy when Petrosian magnitudes were provided (Table 3.7). This is most probably because Petrosian magnitudes are designed to be distance-independent (Petrosian, 1976). Another potential explanation for this occurrence is the fact that when colors are calculated from magnitudes, we are only giving the model four data points instead of five (from magnitudes). In our efforts to give the model better data, then, we may be removing some photometry data (perhaps even indications of luminosity or surface brightness) hidden within the data that the model has found to be relevant, and that we ourselves have not fully identified yet. The subsequent improvements were therefore conducted using the magnitudes as inputs instead of the colors; however, if a distance-independent model were desired, a quick substitution of input files would make all these models function smoothly on color data, without much loss of accuracy (~2% here). All these various input files, as well as code for the models themselves, are freely available on GitHub for further experimentation.

4. Conclusions and Future Work

This project has developed several new models for the morphological classification of elliptical and spiral galaxies, based on a combination of photometric properties, spectra, velocity dispersion, ellipticity, and surface brightness parameters. Six models have been built: Random Forests classification algorithm with bootstrapping implemented (96.28% testing accuracy), Supervised Artificial Neural Network (94.13% testing accuracy), Decision Trees (94.39% testing accuracy), Support Vector Machines (93.42% testing accuracy), K-Nearest-Neighbor Classifier (90.28% testing accuracy), and a Naïve Bayes Classifier (69.87% testing accuracy). Random Forests, Decisions Trees, and K-Nearest-Neighbor classification provided the most time-effective classification without significant loss of accuracy, and Random Forests were optimal in both speed and accuracy. Considerable accuracy can be achieved even when using only photometric parameters, only spectra, or a combination of the two, meaning that galaxies need not undergo many complex algorithms within the advanced SDSS pipelines in order to be classified to a high degree of accuracy. Eventually, this morphology parameter can just be another calculation within the SDSS pipelines.

Environment Density	Training Acc.	Testing Acc.
Included	0.8623	0.8334
Not Included	0.9322	0.8962

Table 3.6: SVM accuracy with and without environment density.

Photometric input	Training Acc.	Testing Acc.
Color	0.8846	0.8579
Petrosian Magnitudes	0.9009	0.8830

Table 3.7: SVM accuracy with color or magnitude.

The next step in future work in the project would be to extend the classification from just a binary system to a more complex classification scheme according to the Hubble Sequence, including identifying barred spirals and irregular galaxies. However, another future direction for further classification could be to use clustering and unsupervised techniques to find classes of galaxies connected in ways that even human visual inspection may not detect. This could potentially serve as an alternate form of galaxy morphology or complement the Hubble Sequence; in any case, it will tell us more about similar galaxies and help us understand their origins better.

Finally, there is even more tuning of parameters and exploration of new inputs to be conducted. While this project was a comprehensive survey of many classification techniques, now that the most effective techniques have been isolated, the focus can be shifted to tuning the parameters and implementing new techniques for more accuracy, speed, efficiency, and less overfitting. The K-Nearest-Neighbor classification algorithm showed the most unexpectedly accurate classification without any tuning of parameters at all, and it is suggested that future work begin by tuning the parameters of this model, optimizing it, and testing it further. The Support Vector Machine can also benefit greatly from further tuning of hyper-parameters. However, this model is particularly difficult to test due to the large amount of time it takes to train. Alternatively, the algorithms with the fastest running times, namely the Decision Trees, Random Forests, and K-Nearest-Neighbor algorithms, can be optimized even more precisely and in far less time. While it is true that the Naïve Bayes classifier trains fastest, the three algorithms mentioned above do a much better job of minimizing time while maximizing accuracy, which is why they are strongly recommended for follow-up research.

The models built in this project can be used without any further modification on all future SDSS data releases to classify galaxies for researchers to use in their investigations of galaxy formation and other fields. For researchers who wish to adapt this model to future galaxy surveys or other classification tasks, they need only make small modifications to the software written for this project, which is freely available to all on GitHub. Data extracted from the SDSS DR7 and Galaxy Zoo data were combined into several different input files, most of which are also in the same GitHub repository (some files are too large for GitHub to store), and all of which are freely available through shared cloud file storage services. Hopefully, the information provided in this successful creation and evaluation of a new model for morphological classification will provide the scientific community with what it needs to study galaxy formation and evolution more thoroughly than ever before, and bring us closer to solving the mystery of how the universe became what it is today.

5. References

Banerji, Manda, Lahav, O., Lintott, C. J., Abdalla, F. B., Schawinski, K., Bamford, S. P., Andreescu, D., Murray, P., Raddick, M. J., Slosar, A., Szalay, A., Thomas, D., Vandenberg, J. (2009). Galaxy Zoo: reproducing galaxy morphologies via machine learning. *MNRAS* **406**, 342–353.

Conselice, Christopher J., Blackburne, J. A., Papovich, C. (2005). The Luminosity, Stellar Mass, and Number Density Evolution of Known Morphology from Z = 0.5 - 3. *ApJ* **620**, 564-583.

de la Calleja, Jorge, Fuentes, O. Machine learning and image analysis for morphological galaxy classification (2004). MNRAS 349 87–93. Dressler, A. (1980). Galaxy morphology in rich clusters–implications for the formation and evolution of galaxies. *ApJ* **236**, 351-365.

Graham, Matthew J., Djorgovski, S. G., Mahabal, A. A., Donalek, C., Drake, A. J. (2013). Machine-assisted discovery of relationships in astronomy. *MNRAS* **000**, 0-15.

Ivezić, Ž. Lupton, R. H., Zinn, R.(2005). The selection of RR Lyrae stars using single epoch data. *AJ* **129**, 1096-1108.

Ivezić, Ž. Connolly, A. J., VanderPlas, J. T., Gray, A. (2014). Statistics, Data Mining, and Machine Learning in Astronomy. *Princeton University Press*.

Kennicutt R.C. (1992). *ApJS* **79**, 255.

Lahav, O., Naim, A., Buta, R. J., Corwin, H. G., de Vaucouleurs, G., Dressler, A., Huchra, J.P., vandenBergh, S., Raychaudhury, S., Sodre, L., Jr., Storrie-Lombardi, M.C.(1995) *Sci*, **267**, 859.

Lahav O., Naim A., Sodre L. Jr, Storrie-Lombardi M. C. (1996). *MNRAS*, **283**, 207.

Lintott, Chris, Schawinski, K., Slosar, A., Land, K., Bamford, S., Thomas, D., Raddick, M. J., Nichol, R. C., Szalay, A., Andreescu, D., Murray, P., Vandenberg, J. (2008). Galaxy Zoo: morphologies derived from visual inspection of galaxies from the Sloan Digital Sky Survey. *MNRAS* **389**, 1179-1189.

Lintott, Chris, Schawinski, K., Slosar, A., Land, K., Thomas, D., Edmondson, E., Masters, K., Nichol, R. C., Raddick, M. J., Szalay, A., Andreescu, D., Murray, P., Vandenberg, J. (2011). Galaxy Zoo 1: data release of morphological classifications for nearly 900 000 galaxies. *MNRAS* **410**, 166-178.

Marzke, Ronald O., Da Costa, L. Nicolaci N., Pellegrini, Paulo S., Willmer, Chirstopher N. A., Geller, Margaret J. (1998). *ApJ* **503**, 617-631.

Naim A., Lahav O., Sodre L., Jr, Storrie-Lombardi M. C. (1995). *MNRAS*, **275**, 567.

Petrosian, Vahe. (1976). Surface brightness and evolution of galaxies. *ApJ* **209**, L1-L5.

Rumelhart, D.E., Hinton, G. E., Williams, R. J. (1986). Learning Internal Representations by Error Propagation. *MIT Press*, Parallel distributed processing: explorations in the microstructure of cognition, **vol. 1**, 318-362.

Srivastava, Nitish, Hinton, G., Krizhevsky, A., Sutskever, I., Salakhutdinov, R. (2014). Dropout: A Simple Way to Prevent Neural Networks from Overfitting. *JMLR* **15**, 1929-1958.

Storrie-Lombardi M. C., Lahav O., Sodre L., Jr, Storrie-Lombardi L. J. (1992). *MNRAS*, **259**, 8.

van den Bergh, Sidney. (1998). Galaxy Morphology and Classification. *Cambridge Univ. Press*, Cambridge.

van der Wel, Arjen. (2008). The Dependence of Galaxy Morphology and Structure on Environment and Stellar Mass. *ApJ* **675** L000-L000.

York, Donald G., and The SDSS Collaboration. (2000). The Sloan Digital Sky Survey: Technical Summary. *AJ* **120**, 1579-1587.

Ultrasonic Fatigue Testing and Crack Initiation in Meso-scale Cantilevers of Ni 718 Superalloy

Isaac A. Cabrera[1], Dr. Jicheng Gong[2], Prof. Angus J. Wilkinson[2]

[1]Student Contributor, Class of 2017, Department of Materials Science and Engineering, Massachusetts Institute of Technology (MIT), Cambridge, MA 02139, USA

[2]Department of Materials, University of Oxford, Parks Road, Oxford OX1 3PH, UK

Meso-scale cantilevers of Nickel 718 were simulated utilizing ABAQUS™ to calculate the resonant frequencies of various geometries as well as to calculate the magnitude of stresses acting on these systems. These cantilevers were then loaded into an ultrasonic testing apparatus that operated at nearly 20 kHz and were cycled between 10^5 and 10^8 times. In situ observations allowed for the cracks to be identified as soon as they formed. Interestingly, large metal extrusions were clearly being formed on these fatigue crack nucleation sites. The samples were imaged utilizing high resolution electron backscatter diffraction (EBSD) to understand how the crack nucleation sites and the crack path related to the microstructure. Similar to other nickel superalloys, fatigue cracks initiated on {1 1 1} slip planes near Σ3 twin boundaries in grains that had high Schmid factors.

1. INTRODUCTION

Ni 718 is the most widely used superalloy in aircraft gas turbine engines. It is used for critical rotating components, compressor airfoils, and other structural forgings. In fact, Ni 718 comprised 34% of the total weight of finished General Electric (GE) CF6 family engines. As of 2001, it comprised 56% of all forgings used by GE Aircraft Engines. It is the material of choice for applications operating up to 650°C because it offers excellent high temperature strength and creep resistance, as well as good corrosion resistance and weldability. What sets Ni 718 apart from other nickel superalloys, such as René 41, is that it can supply all of these properties at a reasonable cost because it is relatively easy to manufacture (Schafrik et al., 2001).

Aircraft engines experience high rates of rotation, large thermal cycles, and frequent restarts. Each of these processes applies a great deal of stress to engine components thus it is easy to understand why these engine components are susceptible to fatigue failures. Fatigue failures are usually characterized by three stages: incubation, initiation, and propagation. Incubation and initiation account for a large portion of the fatigue life and are closely related to each other. Heterogeneities in the microstructure cause plastic deformation to localize during the incubation period. Eventually, after enough cycles, microcracks initiate at the sites of localized plastic strain. Once the cracks have initiated, they typically grow under repeated loading until they reach a critical length after which they grow spontaneously and catastrophically (Roylance, 2001).

Fatigue cracks typically initiate on the surface of a material at large features such as pits, notches, and inclusions. In the absence of such defects, they can initiate on grain boundaries or along persistent slip bands. When initiation occurs below the surface of a material, it usually occurs at voids or near inclusions (Stein et al., 2014). Nickel based superalloys have very few metallurgical defects, thus the cyclic strain localization will occur at heterogeneities in the microstructure. Fatigue cracks have been reported to initiate on large grains and large grain clusters favorably oriented for slip, and they have also been reported to initiate on twin boundaries (Miao et al., 2009).

Previous work by Ma et al. (2010) shows that we should not assume that the s-n curve of Ni 718 reaches a horizontal asymptote beyond 107 cycles. Using conventional methods, they found that specimens fractured even after 108 cycles. It took them more than 40 days to test each sample, thus, it is impractical to utilize conventional fatigue tests in the very high cycle regime. Ultrasonic techniques offer a promising approach to accelerate tests and to achieve very high cycle fatigue failure within a reasonable timeframe (Shyam et al., 2004). At 20 kHz, a common frequency for ultrasonic fatigue testing, 107 cycles can be achieved in just over 8 minutes, 108 cycles can be achieved in about an hour and a half, and 109 cycles can be achieved within 14 hours. Thus very high cycle fatigue behavior can be observed directly to give a true indication of expected service life instead of just extrapolating data from low cycle fatigue behavior.

2. MATERIALS

2.1 Ni 718 Properties

Ni 718 has a nominal composition of 53 (weight) % Ni, 19% Cr, 18% Fe, 3% Mo, 5% Nb, 1% Ti, 0.5% Al, 0.05% C and 0.005% B. Fully heat-treated wrought Ni 718 consists of a γ matrix with γ' and γ" precipitate phases as well as some NbC carbides and TiN nitrides (Krueger, 1989). The primary strengthening phases in Ni 718 are the γ" Ni3Nb phase

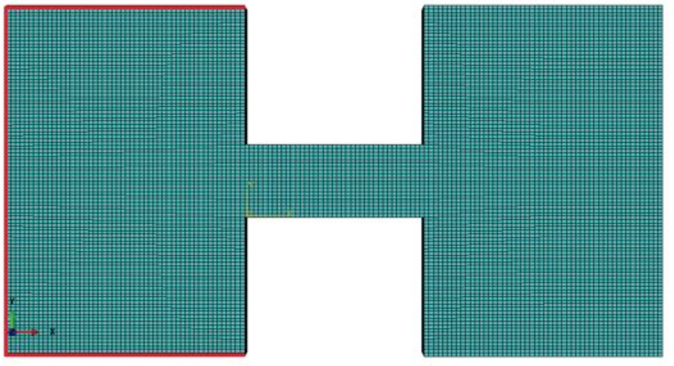

Figure 1: Simplified geometry used in the ABAQUS^{TM} simulations, shown here with a fine mesh. The sides marked in red denote that those positions are fixed.

and the γ' Ni3(Al, Ti) phase. The γ" Ni3Nb phase is the main strengthening phase, has a DO22 crystal structure, and can be identified by the disc shaped precipitates which are between 20 and 40 nm in diameter. The γ' Ni3(Al, Ti) phase has a L12 crystal structure and can be identified by its spherically-shaped precipitates which are 20nm or smaller (Radavich, 1989; Krueger, 1989). Ni 718 has a density at room temperature of 8.22 g/cm3, a Young's Modulus of 200 GPa, and a Poisson's ratio of 0.294 (Alloy 718 Data Sheet).

3. METHODS

3.1 ABAQUS^{TM} Simulations

3.1.1 Grid Generation and Independence

In order to aid the computation process, the simulated cantilever geometry was simplified into the symmetric form visible in Figure 1. The dimensions of each simulated cantilever can be found in Table 1. Using ABAQUS^{TM}, three computational meshes were generated for Geometry 5 in order to perform a grid independence test: a rough mesh consisting of 11,450 hex elements, a fine mesh consisting of 90,800 hex elements, and a very fine mesh consisting of 736,160 hex elements. The corresponding global size for each mesh was $2*10^{-5}$ m for the rough mesh, $1*10^{-5}$ m for the fine mesh, and $5*10^{-6}$ m for the very fine mesh. The grid independence test revealed that the fine mesh was sufficient to gain an accurate estimate of the resonant frequency and the maximum stress thus the rest of the meshes for the other geometries were generated using a global size of $1*10^{-5}$ m.

3.1.2 Resonant Frequency and Dynamic Stress Calculations

Several simulations were performed before fatigue testing began in order to understand what the resonant frequency of each cantilever would be, as well as what the magnitude of the maximum stress experienced by each cantilever would be. The resonant frequency of each cantilever was calculated by running a Linear Perturbation→Frequency procedure and requesting 20 eigenvalues. The maximum stress on each cantilever was calculated by running a Linear Pertubation→Steady State Dynamics→Direct procedure. Two sets of simulations were run to calculate the maximum stress. The first set of dynamic stress simulations compared all of the geometries at a fixed displacement of 10μm and at three frequencies: 19 kHz, 20 kHz, and 21 kHz. The second set of dynamic stress simulations calculated the maximum stress of Geometry 1 at displacements of 1 μm and 2 μm and at 7 frequencies: 19 kHz, 19.5 kHz, 20 kHz, 20.5 kHz, 21 kHz, 21.5 kHz, and 22 kHz. The three boundaries marked in red in Figure 1 were set as fixed for all of the simulations.

Dimensions	H1 (μm)	W1 (μm)	H2 (μm)	W2 (μm)
Geometry 1	1006 ± 2	614 ± 2	206 ± 3	592 ± 2
Geometry 2	1006 ± 3	614 ± 2	206 ± 2	493 ± 2
Geometry 3	1007 ± 3	616 ± 2	209 ± 2	388 ± 1
Geometry 4	1009 ± 2	515 ± 1	207 ± 2	387 ± 2
Geometry 5	1006 ± 4	414 ± 1	207 ± 1	389 ± 1

Table 1: Dimensions of the cantilevers simulated. These dimensions were gathered by measuring previously laser-cut samples.

3.2 Experimental Trials

3.2.1 Sample Preparation

50 samples with 5 separate geometries were laser cut out of a 102μm thick sheet of Ni718 and took the form seen in Figure 2. Of the four specified parameters for the cantilevers, only the head width and neck width varied; the head height and neck height remained constant in all of the geometries. The Ni 718 samples were then electropolished to remove the residual surface stresses as well as to highlight the individual grains. The electropolishing took place at a temperature of -45°C, at a voltage of 35V, and in a solution consisting of 59% methanol, 35% ethylene glycol butyl ether, and 6% perchloric acid. The cantilever disks were first inserted into the electrolyte solution and held in place for 15 seconds before being cleaned in methanol and distilled water. Following electropolishing, the samples were cleaned with a Fischione model 1020 plasma cleaner to remove any residual particles.

3.2.2 Ultrasonic Fatigue Testing

The fatigue crack initiation took place within the apparatus shown in Figure 3. This apparatus consisted of a piezoelectric ultrasonic transducer coupled with a booster which was used to control the vibrational amplitude. The cantilever disks sat in the apparatus parallel to the ground such that cantilever deflected only in the vertical z-axis. Several different boosters gave a combined range of displacements between 0.4 μm and 90 μm; however, the experimental displace-

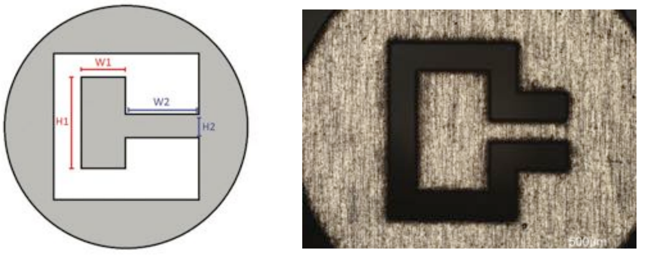

Figure 2: *Left Image* - Schematic showing the general layout of the meso-scale cantilever with the parameters controlled during laser cutting. *Right Image* – An actual cantilever used in the experiments (Cantilever Geometry 1 Sample A1).

Figure 3: Experimental apparatus used to generate fatigue cracks.

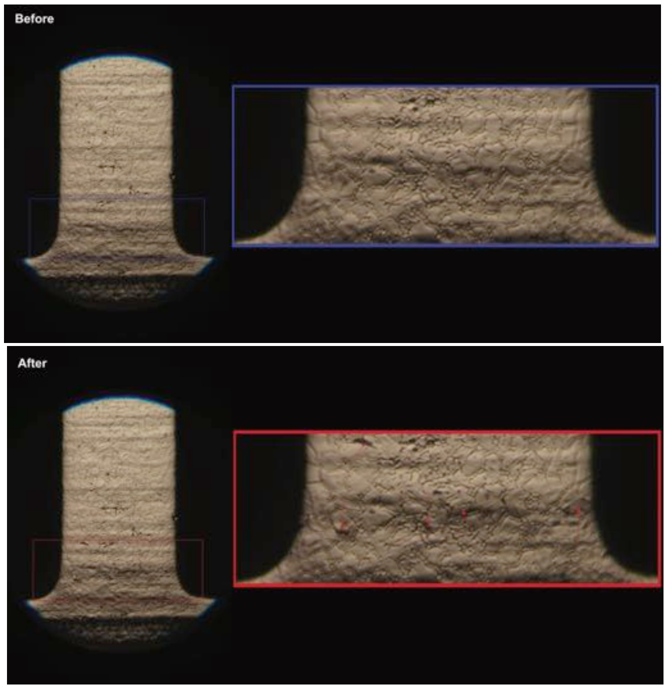

Figure 4: In situ observations of crack growth on sample G1. The top half of the image shows the sample before a crack propagated and the bottom half shows the sample after a crack propagated on the surface.

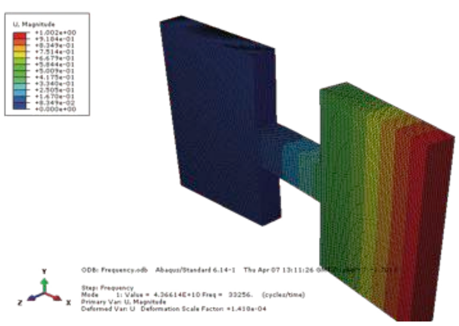

Figure 5: First resonant frequency and vibrational mode calculated for Geometry 4. All of the geometries had a similar-looking first vibrational mode.

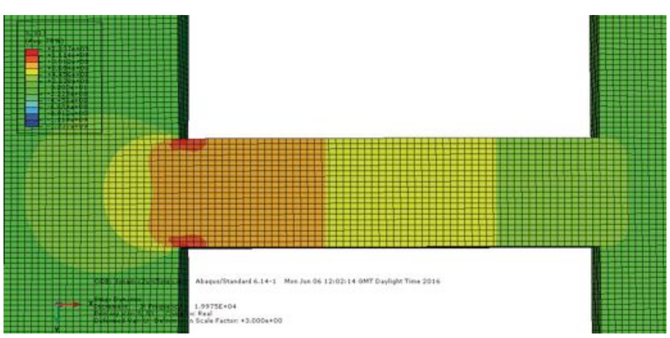

Figure 6: Stress field calculated for cantilever Geometry 1 at a 2 μm displacement and 20 kHz input frequency. All of the stress fields calculated for the other geometries at different frequencies and displacements took a similar form. It is important to note here that the stress field has the highest value near the fixed end of the cantilever.

ments were all less than 5 μm. To initiate the fatigue cracks, the cantilevers were vibrated in increments of 106 cycles starting at a displacement of 0.4 μm. The vibrational amplitude was increased by 0.2 μm with each increment and most cantilevers failed between the 1 μm and 2 μm displacements ($4*10^6$ and $9*10^6$ cumulative cycles respectively.)

In-situ observations were made possible by utilizing a Sony ILCE-5000 digital camera that was paired with a 40x objective lens. The in-situ observation of a cantilever sample before and after the fatigue crack initiation can be seen in Figure 4. During these crack initiation trials an interesting phenomenon occurred; once a small crack had nucleated, metal slivers were extruded out of the face of the material. This was a clear sign of a crack forming and gave an indication of when to stop cycling the cantilevers.

3.2.3 Crystallographic Mapping

Following the crack initiation trials, the Ni 718 cantilevers were imaged using a Zeiss Merlin scanning electron microscope (SEM) and then mapped using a Bruker QUANTAX EBSD detector. Due to the time constraints associated with the EBSD mapping, only 4 samples from Geometry 1 were imaged and mapped. Crystallographic analysis was performed using the Bruker Esprit 2.0 software as well as with Mathematica.

4. Results and Discussion

4.1 ABAQUS™ Simulations

4.1.1 Resonant Frequency Calculations

The resonant frequency of each cantilever was calculated in order to understand which geometry would have the strongest coupling to the ultrasonic vibrator. Figure 5 shows the motion of first vibrational mode; this is the most likely motion of each cantilever because the mode occurs at a frequency closest to the input frequency. Additionally, this mode has only one degree of freedom, which matches the displacement of the cantilever. Geometry 1 had a resonant frequency quite close to 20 kHz so this geometry was expected to have the strongest response in the dynamic stress calculations. As evident in Table 2, the remaining geometries had resonant frequencies that were much higher than 20 kHz, thus we expect that these cantilevers would have a much weaker response to a 20 kHz input.

	Resonant Frequency (Hz)
Geometry 1	20444
Geometry 2	23569
Geometry 3	27817
Geometry 4	33256

Table 2: Results of the resonant frequency calculations. Geometry 1 has the closest resonant frequency to the ultrasonic vibrator.

4.1.2 Dynamic Stress Calculations

In order to avoid breaking the cantilevers and to control the growth rate of the fatigue cracks, it was necessary to determine what the maximum stress values on each cantilever at a certain displacement was. Figure 6 shows the stress field that was encountered in each of the dynamic stress calculations. The highest stress concentration occurs at the corners of the cantilever near the fixed end. It is important to note here that the corners of our simulated fixed end are sharp, whereas the corners on the physical sample are rounded. This would slightly shift the stress concentration to the end of the radius of curvature on the rounded corner. Thus, we can expect that in the real experiments cracks will almost certainly propagate from that region. As evident in Table 3, Geometry 1 had a much higher stress response at all three frequencies than the remaining geometries. Interestingly, the maximum stress decreased at the highest frequency for Geometry 1 whereas

Dynamic Stress Calculations		
Geometry 1	Frequency (Hz)	Max Stress (MPa)
	19000	2014
	20000	6684
	21000	6061
Geometry 2	Frequency (Hz)	Max Stress (MPa)
	19000	691.7
	20000	949.6
	21000	1433
Geometry 3	Frequency (Hz)	Max Stress (MPa)
	19000	349.7
	20000	425.6
	21000	529.7
Geometry 4	Frequency (Hz)	Max Stress (MPa)
	19000	218.1
	20000	254
	21000	298.5
Geometry 5	Frequency (Hz)	Max Stress (MPa)
	19000	141
	20000	160.5
	21000	183.4

Table 3: Comparison of maximum stress values at different frequencies and a fixed displacement of 10μm for all sample geometries.

it increased to a maximum value in all the other geometries. This is simply because 20 kHz is closer to the resonant frequency of 20444 Hz than 21 kHz.

Since Geometry 1 had the strongest coupling, additional calculations were performed to see how sensitive it was to slight changes in input frequency. We can clearly see in Figure 7 that the maximum stress values sharply increased as the input frequency neared the resonant frequency and then they sharply dropped off once the resonant frequency was passed. This result is particularly important because it means that any fatigue experiment needs to have a stable operating frequency in order to give valid results. It also means that, ideally, we do not want to operate directly on the resonant frequency but instead we want to operate close to the resonant frequency.

4.2 Experimental Trials

4.2.1 Extrusions as Crack Nucleation Sites

As anticipated by the ABAQUS^{TM} simulations, we can see in Figure 8 that a fatigue crack formed near the fixed end of the cantilever where the stresses were greatest. The metal extrusions are much more clearly visible in this image as they contrast with the largely homogenous background. If we zoom in on one of these extrusions, as in Figure 9, we can see that a crack has formed beneath it. At a first glance from looking at an IPF-Y map, it appears that these extrusions all occur on grain boundaries; however, after measuring the misorientation angle between these grains, it becomes apparent that these are 60° Σ3 twin boundaries. This is not likely a coincidence because over 90% of the intragranular boundaries in the mapped area on all four samples were Σ3 twins. 20 different extrusions were analyzed from the four samples and nearly all of them occurred on a Σ3 twin boundary.

4.2.2 Calculating the Schmid Factor of Grains Displaying Extrusions

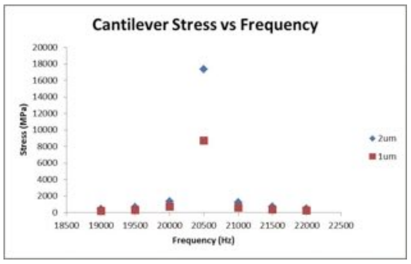

Figure 7: Maximum stress values of Geometry 1 at frequencies ranging from 19 to 22 kHz. The displacement values of 1-2 Microns were chosen in order to have maximum stress values below the yield strength for most of the frequency range.

To get an idea of the degree of shear stress encountered by each extrusion, the Schmid factor was calculated for each of these grains. FCC crystals slip along the {111} family of planes and <-110> family of directions; all of the permutations of these planes and directions yield 12 independent slip systems. The Schmid factor for each slip system was calculated using the formula:

$$Schmid\ Factor = \cos\varphi * \cos\lambda$$

where

$$\cos\varphi = \frac{(Stress\ Direction) \cdot (Slip\ Plane)}{\|Stress\ Direction\| \|Slip\ Plane\|}$$

and

$$\cos\lambda = \frac{(Stress\ Direction) \cdot (Slip\ Direction)}{\|StressDirection\| \|Slip\ Direction\|}$$

Table 4 details the Schmid factors for all 12 slip systems associated with a single grain. It is important to note here that the slip system with the highest Schmid factor is the active slip system. Table 5 details the highest Schmid factors and active slip systems for all the grains showing surface extrusions. It was particularly interesting that in this table all of the grains have the same active slip system (1-11) [011]; however, this could possibly be due to an error in which the Bruker Esprit software saves and displays IPF-Y information. If we look at a Schmid factor map of the entire surface and compare it to a map of where the cracks nucleated, Figure 10, we witness that the cracks and extrusions nucleate almost exclusively on high Schmid factor grains near Σ3 twin boundaries.

Sample	Extrusion	Grain Number	Schmid Factor	Slip System
C1	5	5b	0.367606	(111) [0-11]
			0.212825	(111) [-101]
			-0.154781	(111) [-110]
			0.136407	(-111) [0-11]
			0.318284	(-111) [101]
			0.181876	(-111) [110]
			0.473065	**(1-11) [011]**
			0.143222	(1-11) [-101]
			0.329844	(1-11) [110]
			-0.0309482	(11-1) [011]
			-0.0377625	(11-1) [101]
			0.00681428	(11-1) [-110]

Table 4: Schmid factors for the slip systems associated with grain 5b on sample C1. The bold Schmid factor and slip system denote the active slip system.

4.2.3 Analysis

Previous research on fatigue in nickel superalloys also encountered that cracks and extrusions nucleated on Σ3 twin boundaries (Miao et al., 2009; Stein et al., 2014). This may be surprising because twin boundaries are expected to be low energy and high stability; however, the elastic anisotropy and boundary coherency can allow for stress concentration and slip localization near the twin boundary (Stein et al., 2014). Similar to Stein et al. (2014), these samples cracked on high Schmid factor grains parallel to twin boundaries, but we have not taken into account the effect of slip length. In our case, the Schmid factor calculations are particularly useful to predict which side of the twin boundary the fatigue crack nucleated on. On a grain with an extrusion, the crack is more likely to nucleate on the side with a higher Schmid factor.

Figure 8: High resolution SEM image (500x at 20kV) showing the path of a fatigue crack that formed on the surface of sample G1 after the crack initiation trials.

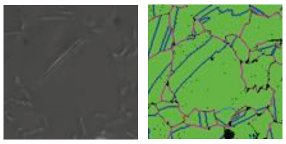

Figure 9: An extrusion and a crack clearly nucleated at this twin boundary on sample C1. *Left Image*: Cropped SEM image of Extrusion 5 C1. *Right Image*: Grain and sub-grain boundary of Extrusion 5 C1. Grain boundaries are denoted with pink and Σ3 twin boundaries are denoted with blue.

Sample	Extrusion Number	Grain Number	Schmid Factor	Active Slip System	Σ3 Twin
C1	5	5b	0.473065	(1-11) [011]	Y
		5t	0.473144	(1-11) [011]	Y
	10	10b	0.494161	(1-11) [011]	Y
		10t	0.497123	(1-11) [011]	Y
	11	11lb	0.489119	(1-11) [011]	Y
		11lt	0.488684	(1-11) [011]	Y
		11rb	0.492484	(111)[0-11], (1-11) [011]	N
		11lt	0.498014	(1-11) [011]	N
E1	1	1b	0.480876	(1-11) [011]	Y
		1t	0.462565	(1-11) [011]	Y
	2	2	0.474145	(1-11) [011]	N
	3	3b	0.459577	(1-11) [011]	Y
		3t	0.495518	(1-11) [011]	Y
	4	4b	0.461901	(1-11) [011]	Y
		4t	0.422077	(1-11) [011]	Y
	5	5b	0.461781	(1-11) [011]	Y
		5t	0.47609	(1-11) [011]	Y
	6	6b	0.46568	(1-11) [011]	Y
		6t	0.462458	(1-11) [011]	Y
	50	50b	0.463278	(1-11) [011]	Y
		50t	0.463267	(1-11) [011]	Y
	64	64b	0.487134	(1-11) [011]	Y
		64t	0.485744	(1-11) [011]	Y
	70	70b	0.488131	(1-11) [011]	Y
		70t	0.488014	(1-11) [011]	Y
G1	1	1b	0.442402	(1-11) [011]	Y
		1t	0.477525	(1-11) [011]	Y
	2	2b	0.460522	(1-11) [011]	Y
		2t	0.461329	(1-11) [011]	Y
	3	3	0.460522	(1-11) [011]	N
	4	4	0.460522	(1-11) [011]	N
	5	5b	0.439803	(1-11) [011]	Y
		5t	0.437583	(1-11) [011]	Y
	6	6b	0.447427	(1-11) [011]	Y
		6t	0.440127	(1-11) [011]	Y
	7	7b	0.452568	(1-11) [011]	Y
		7t	0.452568	(1-11) [011]	Y
	8	8b	0.4858	(1-11) [011]	Y
		8t	0.457842	(1-11) [011]	Y
I1	1	1b	0.440717	(1-11) [011]	Y
		1t	0.443118	(1-11) [011]	Y
	2	2b	0.437703	(1-11) [011]	Y
		2t	0.43812	(1-11) [011]	Y
	3	3b	0.457509	(1-11) [011]	Y
		3t	0.460664	(1-11) [011]	Y
	4	4b	0.494127	(1-11) [011]	Y
		4t	0.49598	(1-11) [011]	Y

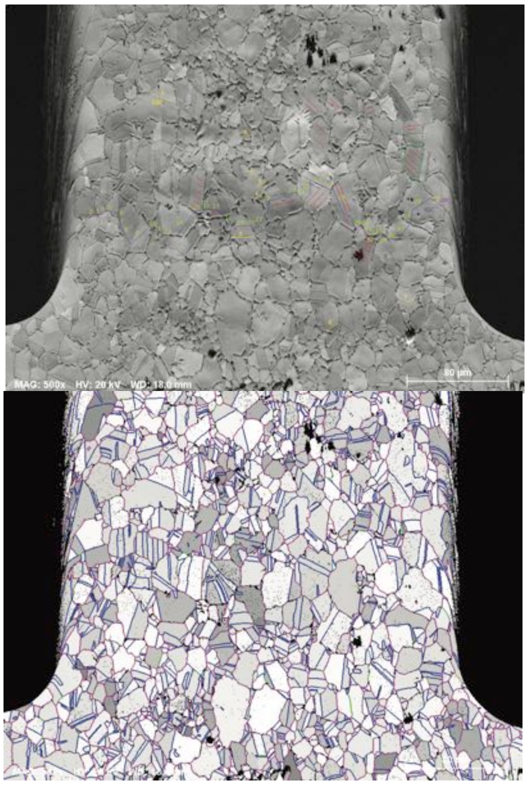

Figure 10: Comparison of an EBSD pattern quality map with the Schmid factor maps for sample G1.

(Far left) Table 5: Schmid factors and active slip systems associated with all of the grains with extrusions. The grains are labeled bottom and top (b and t) because Schmid factor calculations were performed on both sides of the twin boundary within each grain.

6. Conclusions and Future Work

6.1 Conclusions

The ABAQUS™ simulations revealed that the cantilever geometry with a resonant frequency closest to the experimental operating frequency (Geometry 1) would have the strongest coupling and thus encounter the highest maximum stress for a given displacement. The simulations also revealed that these maximum stresses would be localized on the corners near the base of the cantilever. The Ni 718 fatigue tests revealed that extrusions and cracks nucleated on {111} planes in high Schmid factor grains parallel to Σ3 twin boundaries. The most common active slip system in grains exhibiting surface extrusions was the (1-11) [011] slip system. The cracks most likely nucleated on these twin boundaries due to slip localization caused by boundary coherency and the elastic anisotropy of the material.

6.2 Future work

Due to the time limitations imposed on this project, not all of the possible tasks were accomplished for this line of research. Future work should be done to generate s-n curves of the Ni 718; this will require a statistically significant amount of samples of all the same geometry. In addition, serial sectioning should be performed to determine the internal structure of cracks observed on the surface. The cantilevers should be mapped again with EBSD after fatigue testing to generate maps showing the accumulated slip on these twin boundaries. Finally, the correlation between crack nucleation and twin boundary length reported by Stein et al. (2014) should be explored.

7. Acknowledgements

I would like to thank Jicheng Gong and Angus Wilkinson of the Oxford Department of Materials for their guidance and assistance with this research. I would also like to thank Arutyun Arutyunan for his assistance with the data analysis. Finally, I would like to thank Linn Hobbs of MIT and Adrian Taylor of Oxford for facilitating the research program between these two universities.

8. References

Alloy 718 Data Sheet. (n.d.). MAHER. Retrieved from http://www.maher.com/media/pdfs/718-datasheet.pdf

Boehlert, C. J., Li, H., Wang, L., & Bartha, B. (2010, November). Slip System Characterization of Inconel 718 Using In-Situ Scanning Electron Microscopy. Advanced Materials & Processes, 168(11), 41–45.

Cerrone, A., Spear, A., Tucker, J., Stein, C.,Rollet, A., & Ingraffea, A. (2013). Modeling crack nucleation at coherent twin boundaries in nickel-based superalloys. In Multi-scale Modeling of Microstructure Deformation in Material Processing. Montreal, Quebec, Canada.

Krueger, D. D. (1989). The Development of Direct Age 718 For Gas Turbine Engine Disk Applications. In Superalloy 718-Metallurgy and Applications (pp. 279–296). TMS. Retrieved from http://www.tms.org/superalloys/10.7449/1989/Superalloys_1989_279_296.pdf

Ma, X., Duan, Z., Shi, H., Murai, R., & Yanagisawa, E. (2010). Fatigue and fracture behavior of nickel-based superalloy Inconel 718 up to the very high cycle regime. Journal of Zhejiang University-SCIENCE A, 11(10), 727–737.

Miao, J., Pollock, T. M., & Wayne Jones, J. (2009). Crystallographic fatigue crack initiation in nickel-based superalloy René 88DT at elevated temperature. Acta Materialia, 57(20), 5964–5974.

Radavich, J. F. (1989). The Physical Metallurgy of Cast and Wrought Alloy 718 (pp. 229–240).

Roylance, D. (2001). Introduction to Fracture Mechanics. Massachusetts Institute of Technology, Cambridge MA: Department of Materials Science and Engineering.

Schafrik, R. E., Ward, D. D., & Groh, J. R. (2001). Application of Alloy 718 in GE Aircraft Engines: Past, Present and Next Five Years. In Superalloys 718, 625, 706 and various derivatives (pp. 1–11). Warrendale, PA: TMS. Retrieved from http://www.tms.org/superalloys/10.7449/2001/superalloys_2001_1_11.pdf

Shyam, A., Torbet, C. J., Jha, S. K., Larsen, J. M., Caton, M. J., Szczepanski, C. J., … Jones, J.

W. (2004). Development of ultrasonic fatigue for rapid, high temperature fatigue studies in turbine engine materials. In Superalloys 2004 (pp. 259–268). Champion, Pennsylvania: TMS.

Stein, C. A., Cerrone, A., Ozturk, T., Lee, S., Kenesei, P., Tucker, H., … Rollett, A. D.(2014).Fatigue crack initiation, slip localization and twin boundaries in a nickel-based superalloy. Current Opinion in Solid State and Materials Science, 18(4), 244–252.

Design of Rechargeable Battery Packs for a Slocum Glider

Miranda Kotidis[1], Richard Camilli[2],

[1]Student Contributor, Class of 2017, Department of Mechanical Engineering, Massachusetts Institute of Technology (MIT), Cambridge, MA 02139, USA

[2]Associate Scientist, Woods Hole Oceanographic Institution, Deep Submergence Laboratory, Woods Hole, Massachusetts 02543

Rechargeable battery packs, including support structures, were designed and built to replace the existing primary alkaline battery packs in a Slocum underwater glider. The primary alkaline packs supplied approximately 2.29 kW-hr of energy, while the new design provides 2.35 kW-hr (Teledyne Webb Research Maintenance Manual, 2012). The packs also include support structures to maintain the alignment of the batteries while containing them and protecting them during high G-force launch and recovery. These structures feature aluminum and carbon fiber alignment and end plates, held together with titanium tie rods and carbon fiber support tubes. Through simulations and material modeling, the battery packs' support structures were analyzed and are strong enough to survive 5g forces similar to those experienced during the launch and recovery of the vehicle. Prototype battery packs are currently being built, and further work includes custom circuit board development and integration into the vehicle.

Introduction

Slocum gliders are low-power underwater vehicles that can carry payloads designed for ocean data collection, deep sea exploration, and/or military surveillance (Bradley, 1992). Their main form of propulsion comes not from a propeller, but by actively controlling their buoyancy relative to water (Teledyne Webb Research Operator's Manual, 2012). When the vehicle is denser than water, the vehicle sinks and translates this downward motion to forward motion using its wings and control surfaces; similarly, it translates upward motion to forward motion as well when the vehicle is less dense than water (Teledyne Webb Research Operator's Manual, 2012). The duration of the vehicle's deployment is incredibly dependent on the energy stored in the battery packs. The vehicle has two packs, known as the pitch pack and the aft pack. The pitch pack is mounted to a rail system in the fore end of the vehicle and its mass is used to control the pitch of the vehicle (Teledyne Webb Research, 2013). The aft pack is significantly larger and can store more energy, and sits stationary at the aft end of the vehicle. A schematic of the vehicle with the locations of the battery packs is shown in Figure 1.

Gliders currently use alkaline or lithium primary battery packs to power the onboard payloads, sensors, and any onboard propulsion systems. As with any primary battery, the vehicle's battery packs must be replaced when the batteries are drained. To replace the batteries, the vehicle must be disassembled and reassembled with the new primary batteries, and may need to be re-ballasted, a process which must be done in a tank on land. The main advantage of having rechargeable battery packs in an underwater glider is the ability to recharge the batteries without disassembly or re-ballasting, so the vehicle could be recharged at sea. The necessity of bringing the vehicle back to shore every time it needs to have the batteries replaced significantly decreases the duty cycle of the vehicle and makes it incredibly expensive to implement the vehicle in ocean data collection. The duty cycle is a way to measure a system's running time in comparison to its downtime. For this system, the duty cycle can be modeled as:

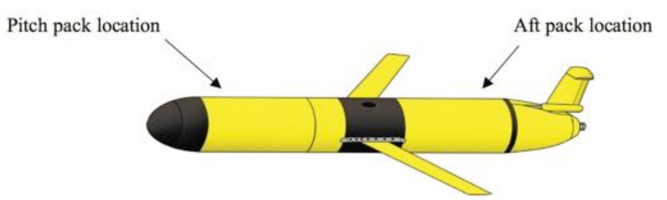

Figure 1: Schematic of the Slocum glider with location of battery packs indicated. The pitch pack is mounted to an actuated rail system used for active controlling of the vehicle's pitch angle, and the aft pack is mounted ridigly to the frame of the vehicle. Image source http://oceanobservatories.org/site/ga05moas-gl.

$$Duty\ Cycle = \frac{Operational\ Time}{Operational\ Time + Time\ to\ replenish}$$

where the operational time is defined as the time spent in the water, using the energy stored in the battery packs to power sensors, payloads, and propulsion mechanisms, and time to replenish is defined as the amount of time from retrieving the glider from the water with drained batteries to when the onboard battery packs are fully ready for another mission. For both types of battery packs, the operational time is defined as follows:

$$Operational\ Time[hr] = \frac{Energy\ stored\ in\ battery\ packs[Whr]}{Power\ usage\ of\ vehicle[W]}$$

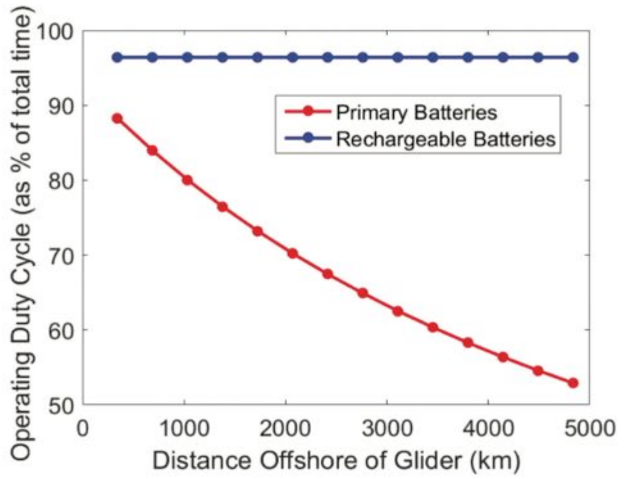

Figure 2: Comparison of duty cycle vs. distance offshore of glider for rechargeable and primary battery packs. The rechargeable battery packs have a more consistent and higher duty cycle than the primary packs.

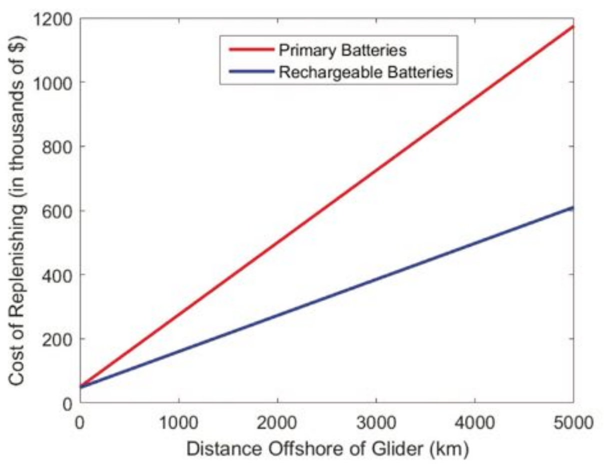

Figure 3: Comparison of cost of replenishing vs. distance offshore of the glider for rechargeable and primary batteries. The rechargeable batteries are a much lower cost option as the glider's mission moves further from the shore.

For the primary battery packs, the time to replenish includes the time to return to shore, replace the batteries, and re-ballast the vehicle. For the rechargeable battery packs, the time to replenish includes the time to recharge the packs. Figure 2 shows the comparison of duty cycle vs. distance offshore of glider for rechargeable batteries and primary batteries, assuming the vehicle uses 10W of power during operation. As the rechargeable batteries can be charged at sea, the time to replenish is much lower. As a result, the duty cycle for the rechargeable batteries is much higher and much more consistent than that of the primary batteries. Figure 3 shows the cost of replenishing vs. distance offshore of glider for rechargeable and primary battery packs. The cost comparison uses the time to recharge value described above and an estimated $50,000/day cost of a research cruise for which the glider would be deployed. As the glider completes missions further from shore, the cost of using primary batteries greatly surpasses the cost of using rechargeable batteries. Overall, replacing the primary battery packs with rechargeable packs allows the underwater glider to be a more useful and cost-effective option for collecting ocean data and underwater surveillance.

Design Requirements

The main requirement for this project was to fully replace the alkaline primary battery packs with rechargeable battery packs. In order to fully replace the alkaline packs, the rechargeable packs must provide at least the same amount of energy to the glider as the alkaline primary packs, about 2.29 kW-hr of energy. The rechargeable packs must also fit in the same volume as the alkaline primary packs without adding extra weight to the vehicle. The support structure for the rechargeable battery packs must mount to the existing glider frame seamlessly. Finally, the support structure for the rechargeable packs must also be strong enough to withstand high G-force launch and recovery commonly experienced by these vehicles during deployment.

Design

The batteries selected for these packs were the Inspired Energy® models NH2034HD34, ND2034HD34, and NH2054HD34. These particular models were chosen for their ability to store high amounts of energy while remaining light and compact, as shown in Table 1 (Inspired Energy, LLC., 2016). The NH2054 model was used in the pitch pack, while the other two models were used in the aft pack, due to their geometry and the space allowed for each pack.

Battery	Volume (in^3)	Weight (g)	Energy stored (W-hr)
NH2034HD34	18.981	435	98
ND2034HD34	9.18	230	49
NH2054HD34	16.74	434	98

Table 1: Comparison of the volume, weight, and energy stored for the batteries used in the design of rechargeable battery packs.

The pitch pack assembly features 10 of the NH2054 batteries, arranged in a circular pattern to maximize the amount of energy stored in this volume, as shown in Figure 4a. This pack provides 0.97 kW-hr of energy to the glider. In order to make sure the batteries remain in place and undamaged, a support frame was built. The pack and the support structure are shown in Figure 4b. The support structure features two carbon fiber plates on either end of the pack, connected by titanium threaded rods acting as tie rods surrounded by carbon fiber tubing for added strength. Aluminum plates were mounted along these rods for the alignment of the batteries and a titanium plate to mount to the glider's frame. Additionally, a custom circuit board was designed to connect the batteries in this configuration while saving as much space as possible. The pack weighs a total 4.95 kg, which is about 47% lighter than the alkaline primary pack. All parts were manufactured using a waterjet cutting machine, or bought directly from a vendor and cut to length.

The aft pack contains 10 of the NH2034 and 8 of the ND2034 batteries, arranged in a semicircular pattern, using the allotted space as efficiently as possible, as shown in Figure 5a. This pack provides 1.37 kW-hr of energy, which, with combined with the pitch pack, supplies a total of 2.35 kW-hr of energy to the glider and onboard sensors. The aft pack assembly and support structure are shown in Figure 5b. Similar to the pitch pack, the aft pack also features a strong support structure to keep the batteries aligned and to support them during glider deployment and missions. The support structure features titanium tie rods surrounded by carbon fiber tubing, carbon fiber support plates and end plate, and an aluminum end plate. The connecting circuit boards were also custom designed to fit perfectly with the battery placement. To mount to the frame of the glider, the pack also features a titanium bracket that connects to the tie rods of the pack. This pack weighs 7.57 kg, which is about 10% lighter than the alkaline primary pack. Similar to the pitch pack, all the parts of this pack were either purchased directly from a vendor or manufactured using a waterjet cutter and cut to length.

During manufacturing, the carbon fiber tubes originally planned for both assemblies proved to be quite weak, as a result of the unidirectional, lengthwise fibers of the tubes. This would have resulted in the carbon fiber tubes to buckle and shatter under compression loads. To solve this problem, these tubes were replaced with woven tubes, which are much stronger in compression.

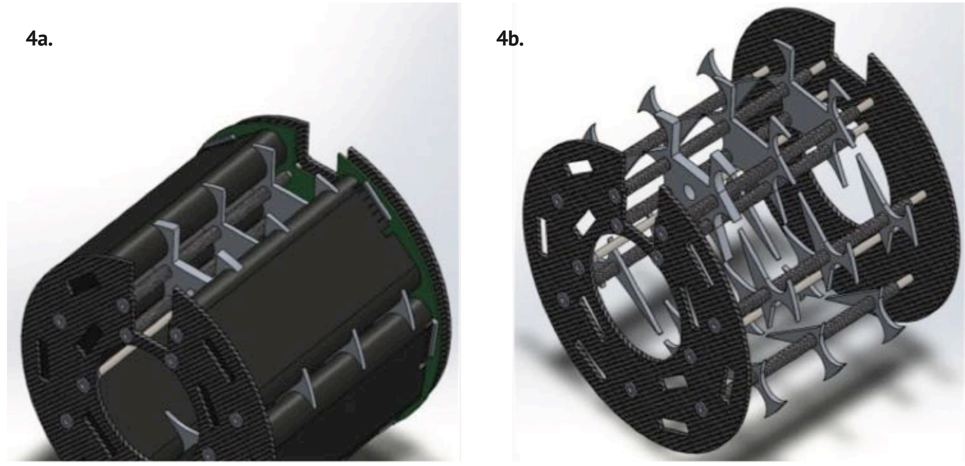

Figure 4a-b: Pitch pack assembly and support structure with the batteries included (a, left) and without the batteries included (b, right).

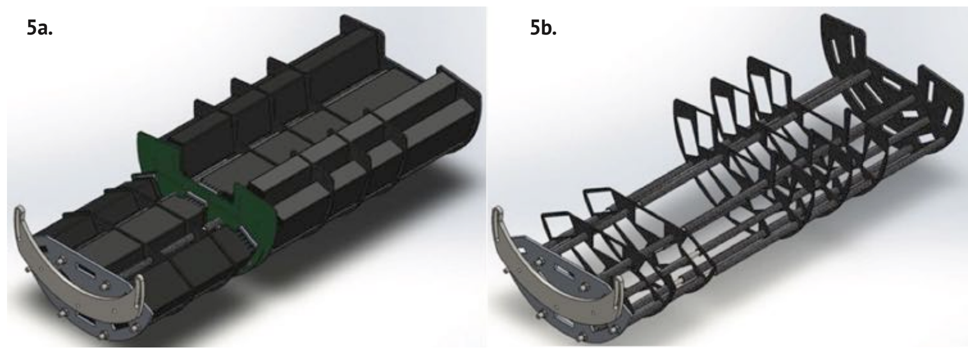

Figure 5a-b: Aft pack assembly and support structure with the batteries included (a, left) and without the batteries included (b, right).

Analysis

Using Finite Element Analysis (FEA) software included in SolidWorks®, the support structure of the pitch pack was tested to ensure the structure would withstand high G-force conditions. Figure 6 shows the pitch pack color map of factor of safety under 332 N of axial force. The minimum factor of safety for this loading condition was 1.89. The frame was also tested with 330 N of force in shear directions, and the minimum factor of safety for those tests was 2.04.

Due to a fault in the FEA software, the aft pack simulation resulted in an inexplicable stress concentration, and modeled high amounts of stress that were unrealistic. This stress concentration was a result of the meshing of the complex assembly, and was unavoidable in the FEA model. In order to verify the strength of the support structure for this pack, the aft pack structure had to be analyzed analytically. Since the aft pack is rigidly mounted on one end, it experiences similar loads and stresses to a cantilever beam, and was modeled as such. The main components of the pack's structure to support this cantilever are the titanium rods, so the pack was modeled as nine (9) titanium rods. In the analysis, the maximum stress and the maximum deflection of the rods while supporting a load were the primary interests. Following classical beam bending analysis, the maximum stress at the mounted end of the rods and the maximum deflection of the rods at the free end can be calculated through the following equations (Unknown, Retrieved 2016).

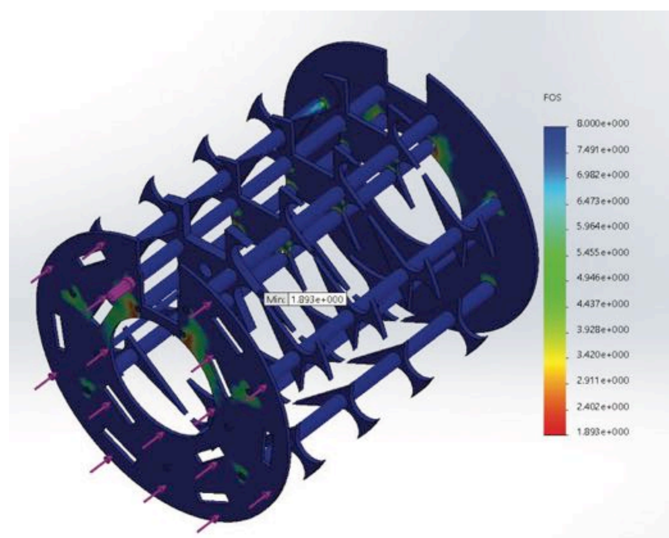

Figure 6: Pitch pack color map of factor of safety under 332 N of axial force. As shown in the legend, the lower factor of safety is equivalent to more stress, and is shown in red.

$$max\ stress = \frac{point\ load * length\ of\ rod}{section\ modulus\ of\ rod * number\ of\ rods}$$

$$max\ deflection = \frac{point\ load * (length\ of\ rod)^3}{Young's\ Modulus\ of\ material * area\ moment\ of\ inertia\ of\ rod}$$

This value of maximum stress was then used to calculate the factor of safety of the loading condition. The factor of safety is a dimensionless number used to measure of the stress distribution compared to the tensile strength of the material, and is used to determine whether the object or assembly in question will or will not fail. The factor of safety is determined by:

$$Factor\ of\ Safety = \frac{Tensile\ Strength\ of\ material}{Maximum\ stress\ of\ loading\ condition}$$

The loading condition was modeled to be 100N of point force applied at the end of the pack. Using the geometry of the pack, and the material properties of the tie rods, the factor of safety of this loading condition was found to be 1.10.

This model overestimates the stress experienced by the pack, as the battery pack design includes additional supports through the carbon fiber tubes and the battery spacers and end plates. As the end plate of the pack would rest against the inside wall of the hull, the hull prevents the packs from large cantilevered deflections, causing the maximum stress at the mounted end of the pack to be much lower, and significantly increasing the factor of safety. If the rods are constrained to deflect by 0.25 in (0.00635 m), the factor of safety becomes 321.

Conclusion

Rechargeable battery packs for a Slocum glider were designed and built to replace the current primary alkaline packs. The rechargeable packs provide 2.35 kW-hr of power, while the primary alkaline packs provided 2.29 kW-hr. The two rechargeable packs, known as the pitch pack and aft pack, feature support structures designed to maintain the alignment of the batteries, while containing and protecting them from damage during high G-force launch and recovery. These structures are made of carbon fiber and aluminum plates held together by titanium tie rods, and also feature custom circuit boards to electrically connect the batteries to the rest of the system while removing complex and messy wired connections. These new packs allow the vehicle to be recharged at sea, whereas the primary packs required complete replacement when the batteries were drained. The process of replacing the primary batteries must be done on shore, as the vehicle may need to be re-ballasted once fresh batteries are installed. This transition to rechargeable batteries dramatically increases the functional duty cycle of the vehicle, and greatly decreases the cost of using a glider for ocean research or other missions. Future work includes manufacturing the custom circuit boards to connect the batteries to sensors and other electronics, and fully integrating the packs into the vehicle for testing.

References

[1] Teledyne Webb Research. (2012). Slocum G2 Glider Maintenance Manual. Retrieved July 2016 from http://gliderfs2.coas.oregonstate.edu/gliderweb/docs/slocum_manuals/Slocum_G2_Glider_Maintenance_Manual.pdf

[2] Bradley, A. (1992). Low Power Navigation and Control for Long Range Autonomous Underwater Vehicles. The Second International Offshore and Polar Engineering Conference.

[3] Teledyne Webb Research. (2012). Slocum G2 Glider Operator's Manual. Retrieved July 2016 from http://gliderfs2.coas.oregonstate.edu/gliderweb/docs/slocum_manuals/Slocum_G2_Glider_Operators_Manual.pdf

[4] Teledyne Webb Research. (2013). Slocum G2 Glider Product Catalog. Retrieved July 2016 from http://www.webbresearch.com/pdf/G2_Product_Catalog.pdf

[5] Inspired Energy, LLC. (2016). Inspired Energy Products Catalog. Retrieved June 2016 from http://www.inspired-energy.com/products.html

[6] Unknown. Bending Stress and Deflection for Cantilevered Beam, Point Load. Retrieved July 2016 from http://www.atcpublications.com/Sample_pages_from_FDG.pdf